Open Ceramics 6 (2021) 100099

Contents lists available at ScienceDirect

Open Ceramics

journal homepage: www.editorialmanager.com/oceram

# Growth of single crystals of $0.75(Na_{0.5}Bi_{0.5})TiO_3$-$0.25(Sr_{0.7}Ca_{0.3})TiO_3$ and characterisation of their electrical properties

Phan Gia Le [a,1], Thi Lan Tran [a], Hwang-Pill Kim [b], Wook Jo [b], Jong-Sook Lee [a,**], John G. Fisher [a,*]

[a] School of Materials Science and Engineering, Chonnam National University, Gwangju 61186, Republic of Korea
[b] School of Materials Science and Engineering, Ulsan National Institute of Science and Technology, Ulsan 44919, Republic of Korea

ARTICLE INFO

*Keywords:*
$(Na_{0.5}Bi_{0.5})TiO_3$
Lead-free piezoelectric
Single crystal

ABSTRACT

Single crystals of $0.75(Na_{0.5}Bi_{0.5})TiO_3$-$0.25(Sr_{0.7}Ca_{0.3})TiO_3$ (NBT-25SCT) were grown by top-seeded solid state crystal growth. X-ray diffraction of a polycrystalline ceramic sample and Raman scattering of a single crystal reveal that rhombohedral symmetry is predominant in the structure. The relative permittivity curves of (001), (110) and (111)-oriented single crystals show them to possess relaxor ferroelectric behaviour. The polarization vs. electric field and bipolar strain vs. electric field behaviour of the crystals differ greatly depending on crystallographic orientation. NBT-25SCT single crystals with (111) and (110) orientation show typical ferroelectric/piezoelectric behaviour whereas the (001) orientation initially shows electrostrictive behaviour followed by ferroelectric/piezoelectric behaviour at higher electric fields. Parametric impedance modelling over a wide temperature range is performed by considering mixed ionic and electronic conduction as well as universal dielectric response behaviour. The fitted parameters can represent the features of the raw data, allowing identification of the transition points and associated processes.

## 1. Introduction

Nowadays, $(Na_{0.5}Bi_{0.5})TiO_3$ (NBT)-based piezoelectric materials are being intensively studied to seek new lead-free materials possessing superior electrical properties, in order to replace lead-based piezoelectric materials because the toxicity of lead causes damage to the environment as well as to human health [1–6]. Compositions based on the (1-x)$(Na_{0.5}Bi_{0.5})TiO_3$-x$SrTiO_3$ (NBT-ST) solid solution are receiving increasing attention due to their extraordinary inverse piezoelectric properties caused by an electric field-induced relaxor to ferroelectric phase transition [7–13]. For example, a strain of 0.29% at an electric field of 4 kV/mm was reported by Acosta et al. [8] for the composition $0.75(Na_{0.5}Bi_{0.5})TiO_3$-$0.25SrTiO_3$ (NBT-25ST). Afterwards, many material systems were constructed based on the NBT-ST solid solution to enhance both structure and electrical properties to find out the materials with excellent properties and capability for practical application as an actuator [14–20]. In order to enhance microstructure as well as electrical properties, NBT-ST compositions were doped with various elements to substitute on the A site or B site. For example, Malik et al. found an improvement in strain to S = 0.438% at E = 5 kV/mm corresponding to $d^*_{33}$ = 876 pm/V with Nb doping of a $Bi_{0.5}(Na_{0.84}K_{0.16})_{0.5}TiO_3$–$SrTiO_3$ composition [21].

Single crystals of NBT-based compositions show better electrical properties in comparison to ceramics with the same composition, due to the improved alignment of the ferroelectric domains in the poling field or improved polarization extension in the applied electric field [22–26]. Single crystals in the NBT-ST system have previously been grown by solid state crystal growth [27–29] and NBT-25ST single crystals were found to have improved inverse piezoelectric properties [30]. However, growth rate of the single crystals is restricted by excessive grain growth in the matrix, which reduces the driving force for single crystal growth [31]. Compared to the NBT-ST system, $0.96(Na_{0.5}Bi_{0.5})TiO_3$-$0.04CaTiO_3$ showed improved solid state single crystal growth [32]. This raised the possibility of improving the growth rate of NBT-25ST by substituting Sr with Ca. Indeed, in previous work, we found that partially substituting Sr with Ca in the $0.8(Na_{0.5}Bi_{0.5})TiO_3$-$0.2(Sr_{1-x}Ca_x)TiO_3$ system could restrict matrix grain growth, allowing larger single crystals to be grown [33]. In the present work, single crystals of composition $0.75(Na_{0.5}Bi_{0.5})TiO_3$–$0.25(Sr_{0.7}Ca_{0.3})TiO_3$ are grown by the solid state crystal growth method and their crystal structure, ferroelectric and piezoelectric properties are studied in detail.

* Corresponding author.
** Corresponding author.
*E-mail addresses:* jongsook@jnu.ac.kr (J.-S. Lee), johnfisher@jnu.ac.kr (J.G. Fisher).
[1] Current affiliation: Department of BioNano Technology, Gachon University, Seongnam-si, Gyeonggi-do 13120, Republic of Korea.

https://doi.org/10.1016/j.oceram.2021.100099
Received 31 December 2020; Received in revised form 31 March 2021; Accepted 2 April 2021
Available online 6 April 2021

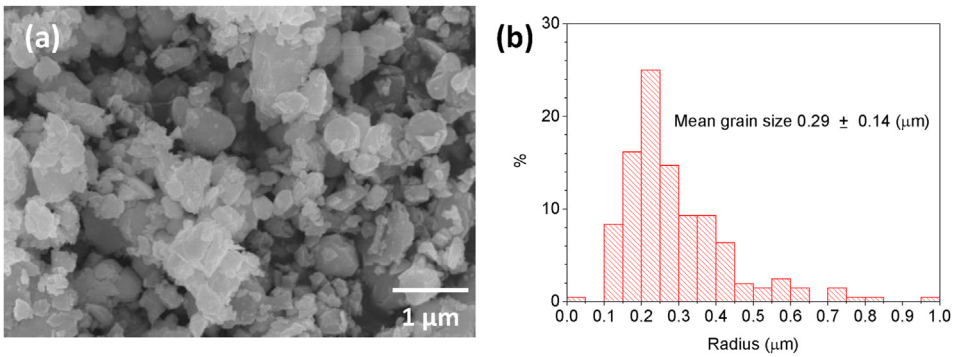


**Fig. 1.** (a) SEM micrograph and (b) particle size distribution of the $0.75(Na_{0.5}Bi_{0.5})TiO_3$–$0.25(Sr_{0.7}Ca_{0.3})TiO_3$ powder after calcination and ball milling.

## 2. Material and methods

The $0.75(Na_{0.5}Bi_{0.5})TiO_3$–$0.25(Sr_{0.7}Ca_{0.3})TiO_3$ (NBT-25SCT) powder is synthesized from $Na_2CO_3$ (ACROS Organics, 99.5%), $Bi_2O_3$ (Alfa Aesar, 99.9%), $TiO_2$ (Alfa Aesar, 99.8%), $SrCO_3$ (Aldrich, ≥ 99.9%) and $CaCO_3$ (Aldrich, ≥ 99.9%) starting materials by the solid state reaction route. The starting materials are dried in an oven at 250 °C for 5 h to remove adsorbed water. The stoichiometrically weighed amounts of these initial materials are mixed and ground in high-purity (99.9%) ethanol in a $ZrO_2$-lined jar in a planetary ball mill (Planetary Micro Mill Pulverisette 7, Fritsch GmbH, Idar-Oberstein, Germany) for 3 h (alternating 5 min milling and 1 min rest intervals) at 500 rpm using $ZrO_2$ media. After milling, the ethanol is evaporated using a hot plate and magnetic stirrer. Then, the slurry is dried in an oven at 80 °C for 12 h to totally remove any remaining ethanol. The dried slurry is ground in an agate mortar and pestle, then sieved through a 180 µm sieve to remove agglomerates. The powder is put into high purity alumina double crucibles with lids and calcined at 900 °C for 3 h in air, with heating and cooling rates of 5 °C/min. The calcined powder is planetary ball milled, ground and sieved again to break up any agglomerates and reduce the particle size. The powder is analysed by X-ray diffraction (XRD, X'Pert PRO, PANalytical, Almelo, the Netherlands) using Cu Kα radiation, a scan range of 20–90° 2θ and a scan speed of 3°/min. A powder sample is Pt-coated and observed by Scanning Electron Microscopy (SEM, Hitachi S-4700, Tokyo, Japan). The particle size distribution of the powder is analysed from the SEM micrographs using imageJ v1.50a image analysis software (National Institute of Mental Health, Bethesda, MD). The area of 200 particles was measured and converted into equivalent spherical 2D radii.

NBT-25SCT single crystals were fabricated by top-seeded solid state crystal growth [32]. Pellets of NBT-25SCT (without a seed crystal) are pressed in a cold isostatic press at 147 MPa, pre-sintered at 900 °C for 1 h and their top faces polished to a 1 µm finish. (110), (001) and (111) oriented $SrTiO_3$ seed crystals (MTI Corp., CA) are then placed on the polished faces of the pellets, the samples are buried in NBT-25SCT powder in a steel die, pressed by hand into pellets and compacted in the cold isostatic press as before. Samples are then sintered at 1250 °C for 20 h, 50 h or 100 h with heating and cooling rates of 5 °C/min. To reduce volatilisation of Na and Bi during sintering, the pellets are buried in a packing powder of the same composition in a double alumina crucible with lids. For comparison, a single crystal was also grown by solid state crystal growth i.e. the seed crystal was buried in the NBT-25SCT powder, pressed into a pellet and sintered at 1250 °C for 20 h without any pre-sintering.

The samples are vertically sectioned using a low speed diamond wheel saw, polished to a 1 µm finish with diamond paste and thermally etched at 1200 °C. The etched samples are Pt-coated and observed by Scanning Electron Microscopy (SEM, Hitachi S-4700, Tokyo, Japan). The mean matrix grain size and grain size distribution is analysed from the SEM micrographs using imageJ v1.50a image analysis software (National Institute of Mental Health, Bethesda, MD). To estimate the mean matrix grain size and grain size distribution, the equivalent 2D radii of at least 200 grains are selected for each sample. To analyze single crystal thickness of the (001)-oriented NBT-25SCT single crystals, the single crystal in each micrograph is divided into slices and the area of each slice measured. By dividing the area of each slice by its width, the average growth distance of the crystal in that slice could be measured. For each sample, the mean and standard deviation of 50 slices are measured. The growth distance of the (110)-oriented NBT-25SCT single crystal was measured at the point of maximum growth. The chemical composition of a (111)-oriented NBT-25SCT single crystal grown at 1250 °C for 20 hours was analysed using Electron Probe Microanalysis (EPMA, JEOL JXA-8530F PLUS, Tokyo, Japan). The sample was polished as before but not thermally etched. Wavelength-dispersive spectroscopy (WDS) analysis was carried out using an accelerating voltage of 15 kV $NaAlSi_2O_6$, $Bi_4Ge_3O_{12}$, $SrTiO_3$ and $CaWO_4$ were used as standards.

For measurement of the electrical properties, single crystals are grown at 1250 °C for 20 h using (110) and (111)-oriented $SrTiO_3$ seed crystals. After growth, (110) and (111)-oriented NBT-25SCT single crystals are removed from the surrounding matrix grains and ground with SiC paper up to grade #2000 until the NBT-25SCT single crystal is exposed on both major faces i.e. until the seed crystal on one face and the matrix grains on the other face are removed. The (001)-oriented single crystals are prepared from a single crystal grown on a (110)-oriented $SrTiO_3$ seed crystal. The seed crystal and surrounding matrix grains are removed and the sample vertically sectioned and ground as before to expose the (001) major faces of the single crystal. To check the orientation, the single crystals are analysed by X-ray diffraction (XRD, X'Pert PRO, PANalytical, Almelo, the Netherlands) using Cu Kα radiation, a 2θ scan range of 20–90°, step size 0.02° and a scan speed of 3°/min. For analysis of the crystal structure, a polycrystalline sample (sintered at 1250 °C for 1 h without a seed crystal) is crushed into powder and analysed by XRD as before.

For micro-Raman scattering, a (111)-oriented single crystal sample grown at 1250 °C for 20 hours is removed from the matrix and seed crystal and polished to a 1 µm finish with diamond suspension on one major face. The sample is then annealed at 400 °C for 1 h and cooled at a rate of 1 °C/min to remove strains generated during polishing. Micro-Raman scattering is carried out with a 514 nm $Ar^+$ ion laser and output power of 10 mW (LabRam HR800 UV Raman microscope, Horiba Jobin-Yvon, France). The Raman spectrum is recorded at room temperature in back scattering geometry with a resolution of ~0.5 $cm^{-1}$. The diameter of the laser spot on the sample is 1–2 µm.

For the impedance spectroscopy measurements, the major faces are coated with Pt-paste and the sample fired in a muffle furnace at 900 °C for 30 min with heating and cooling rates of 5 °C/min. An impedance analyser (HP4284A, Hewlett-Packard, Kobe, Japan) is utilized to record the conductance and resistance of each sample at different temperatures and frequencies. Samples were measured in a hot stage (TS1500, Linkam, Tadworth, United Kingdom) in the temperature range 30–800 °C with heating and cooling rates of 1 °C/min. The AC voltage is set to 0.5 V and

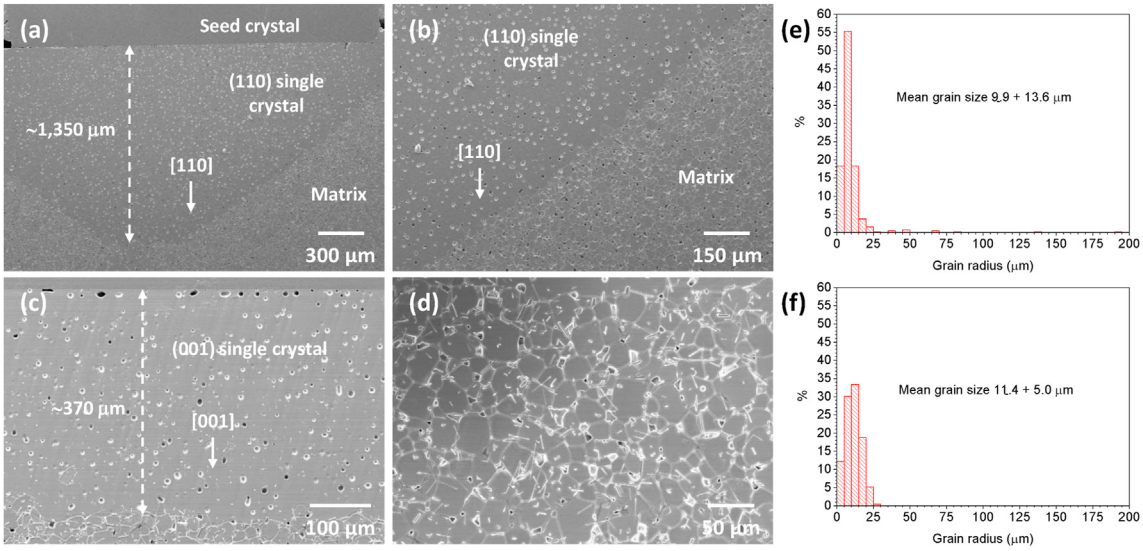


**Fig. 2.** (a, b) SEM micrographs of a $0.75(Na_{0.5}Bi_{0.5})TiO_3$–$0.25(Sr_{0.7}Ca_{0.3})TiO_3$ single crystal grown on a (110)-oriented $SrTiO_3$ seed crystal; (c) SEM micrograph of a $0.75(Na_{0.5}Bi_{0.5})TiO_3$–$0.25(Sr_{0.7}Ca_{0.3})TiO_3$ single crystal grown on a (001)-oriented $SrTiO_3$ seed crystal; (d) SEM micrograph of matrix grains from the (001)-oriented $0.75(Na_{0.5}Bi_{0.5})TiO_3$–$0.25(Sr_{0.7}Ca_{0.3})TiO_3$ single crystal; (e) matrix grain size distribution of the (110)-oriented $0.75(Na_{0.5}Bi_{0.5})TiO_3$–$0.25(Sr_{0.7}Ca_{0.3})TiO_3$ single crystal; (f) matrix grain size distribution of the (001)-oriented $0.75(Na_{0.5}Bi_{0.5})TiO_3$–$0.25(Sr_{0.7}Ca_{0.3})TiO_3$ single crystal.

the frequency range from 31.6 Hz to $10^6$ Hz.

For the ferroelectric and piezoelectric properties, single crystals are prepared as above but are polished on both major faces using SiC paper to a final finish of #4000 grade. The thickness of the samples are ~ 0.8–1.3 mm and the major faces of the samples are approximately parallel to the (110), (001) or (111) planes of the single crystal respectively. Silver paste was screen printed on both sides of the specimens and then dried in a drying oven at 100 °C for 30 min. The external electric field dependencies of polarization (P) and strain (S) hysteresis were measured in a commercial apparatus, aixPES (aixACCT System GmbH, Aachen, Germany) using a bipolar electric field profile with amplitude of up to 7.5 kV/mm at 0.5 Hz.

## 3. Results

An SEM micrograph of the calcined and ball-milled NBT-25SCT powder is shown in Fig. 1 (a). Most of the particles are submicron in size, but some particles of ~ 1 µm diameter are visible. The particle size (radius) distribution is shown in Fig. 1 (b). The particle size distribution is unimodal with a tail out to 1 µm. The mean particle radius and standard deviation for the powder is 0.29 µm ± 0.14 µm. SEM micrographs of NBT-25SCT single crystals grown by top-seeded solid state crystal growth on (110)- and (001)-oriented $SrTiO_3$ seed crystals at 1250 °C for 20 h are shown in Fig. 2. In both cases, a single crystal of NBT-25SCT has grown from the seed crystal into the pellet. The growth rate in the [110] direction is much faster than in the [001] direction. Both single crystals contain porosity. Fig. 2 (d) shows an SEM micrograph of the matrix grains. The matrix grains are equiaxed and many are cuboid in shape, with faceted grain boundaries. A rod-shaped secondary phase is visible in the matrix. This is probably $TiO_2$ or an $Na_2O$-$TiO_2$ compound [30,33]. Fig. 2 (e) shows the matrix grain size distribution of the (110)-oriented single crystal. The grain size (radius) distribution is bimodal with a peak whose mean grain size is 8.2 µm and a small number of much larger abnormal grains up to 190 µm in size. The mean grain size and standard deviation for the entire distribution is 9.9 ± 13.6 µm. Fig. 2 (f) shows the matrix grain size distribution of the (001)-oriented single crystal. The grain size distribution is unimodal. The mean grain size is slightly larger than that of the (110)-oriented single crystal, but no abnormal grains are present.

The EPMA chemical analysis results are shown in Table 1. The results are the average and standard deviation of eight measurement points. The results are given as the mol % of the constituent oxides, assuming oxygen stoichiometry. The nominal composition for NBT-25SCT is also given. The chemical composition of the single crystal is very close to the nominal composition. The single crystal is slightly deficient in Na and slightly excess in Ca and Bi. Sodium deficiency was previously noticed in NBT-25ST single crystals grown by this method [28,30].

**Table 1**
EPMA analysis results of a (111)-oriented $0.75(Na_{0.5}Bi_{0.5})TiO_3$–$0.25(Sr_{0.7}Ca_{0.3})TiO_3$ single crystal.

| Oxide | Average (mol %) | STD (mol %) | Nominal composition (mol %) |
|---|---|---|---|
| $Na_2O$ | 10.77 | 0.15 | 11.54 |
| $Bi_2O_3$ | 11.85 | 0.07 | 11.54 |
| SrO | 10.73 | 0.16 | 10.77 |
| CaO | 4.90 | 0.08 | 4.62 |
| $TiO_2$ | 61.75 | 0.15 | 61.54 |

Fig. 3 (a) shows the single crystal growth distance vs. sintering time. The [110] direction is clearly the fastest growth direction. Even after 100 h of sintering, the (001)-oriented single crystal has only grown ~820 µm, whereas the (110)-oriented single crystal has reached a maximum growth distance of 1350 µm after 20 h. Fig. 3 (b) shows the porosity in a (110)-oriented NBT-25SCT single crystal grown by top-seeded solid state crystal growth for 20 h. For comparison, a (110)-oriented NBT-25SCT single crystal was grown by solid state single crystal growth at 1250 °C for 20 h. From Fig. 3 (c) it can be seen that this single crystal is more porous than the crystal grown by top-seeded solid state crystal growth. Fig. 3 (d) shows Archimedes density measurements of NBT-25SCT single crystals grown by both methods. The theoretical density of NBT-25SCT was calculated to be 5.71 g/cm$^{-3}$ based on unit cell parameters estimated from the XRD pattern for polycrystalline NBT-25SCT. The density of the single crystal grown by top-seeded solid state single crystal growth is higher than that of the single crystal grown by solid state single crystal growth.

NBT-25SCT single crystal samples prepared for electrical property measurements are shown in Fig. 4. Estimated geometry factors are given in Table 2. Fig. 5 shows the XRD patterns of the NBT-25SCT single crystals shown in Fig. 4 and the polycrystalline sample. All patterns are indexed using PDF file #89–3109 for cubic NBT $\left(Pm\bar{3}m\right)$. The

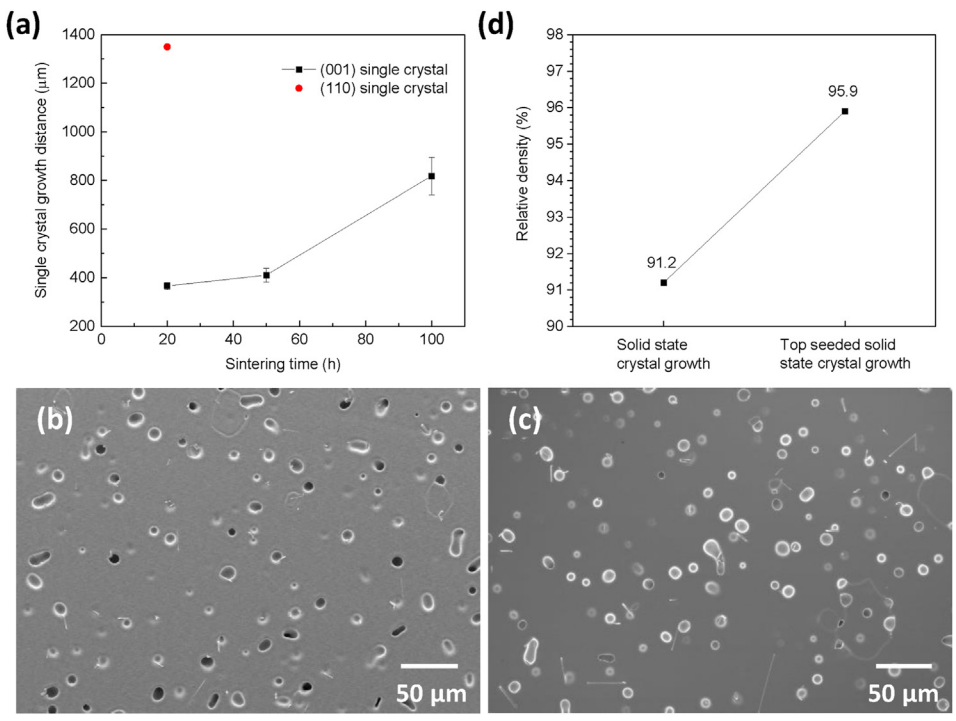


**Fig. 3.** (a) Single crystal growth distance of the (001) and (110)-oriented $0.75(Na_{0.5}Bi_{0.5})TiO_3$–$0.25(Sr_{0.7}Ca_{0.3})TiO_3$ single crystals; (b) SEM micrograph of a (110)-oriented $0.75(Na_{0.5}Bi_{0.5})TiO_3$–$0.25(Sr_{0.7}Ca_{0.3})TiO_3$ single crystal grown by top-seeded solid state crystal growth; (c) SEM micrograph of a (110)-oriented $0.75(Na_{0.5}Bi_{0.5})TiO_3$–$0.25(Sr_{0.7}Ca_{0.3})TiO_3$ single crystal grown by solid state crystal growth; (d) Archimedes density of (110)-oriented $0.75(Na_{0.5}Bi_{0.5})TiO_3$–$0.25(Sr_{0.7}Ca_{0.3})TiO_3$ single crystals grown by solid state crystal growth and top-seeded solid state crystal growth.

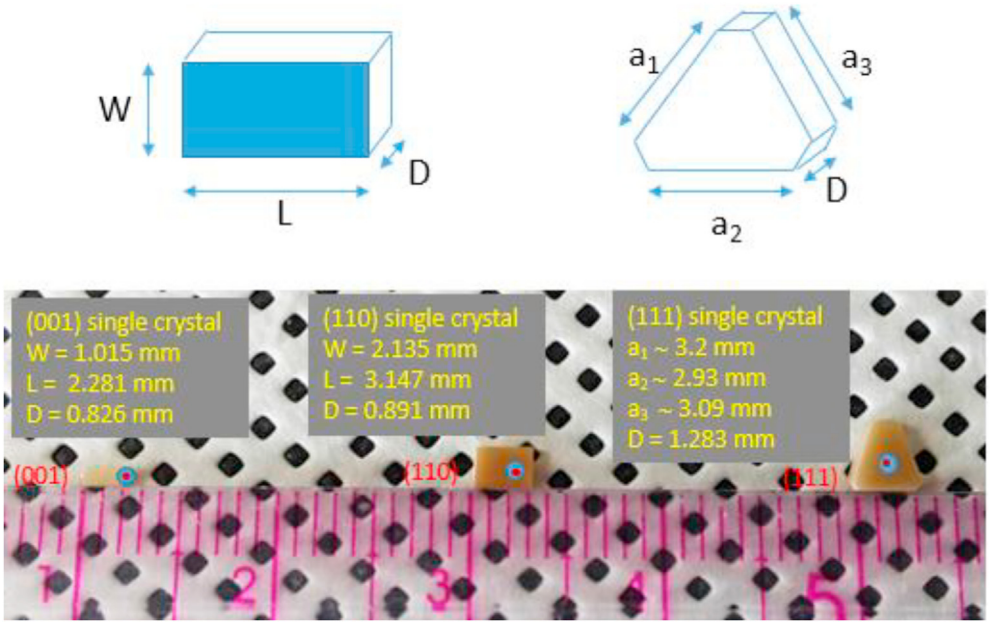


**Fig. 4.** Single crystals of $0.75(Na_{0.5}Bi_{0.5})TiO_3$–$0.25(Sr_{0.7}Ca_{0.3})TiO_3$ grown by top-seeded solid state crystal growth.

**Table 2**
Geometry factors of (001), (110) and (111)-oriented 0.75 $(Na_{0.5}Bi_{0.5})TiO_3$–$0.25(Sr_{0.7}Ca_{0.3})TiO_3$ single crystals for electrical characterization.

| Orientation | A ($cm^2$) | t (cm) | A/t (cm) | A*t ($cm^3$) |
|---|---|---|---|---|
| (001) | 0.0210 | 0.0819 | 0.2564 | 0.0017 |
| (110) | 0.0580 | 0.0878 | 0.6606 | 0.0051 |
| (111) | 0.0680 | 0.0739 | 0.9202 | 0.0050 |

polycrystalline sample shows all possible diffraction peaks for the different crystallographic planes of the NBT structure except for the 221 peak which is too weak to be detected. The single crystal samples only show intense peaks for the (100)/(200), (110)/(220) and (111)/(222) crystallographic planes respectively, showing them to be of (001), (110) and (111) orientation [28–30,34]. The (001)-oriented NBT-25SCT single crystal pattern is very noisy due to the small size of the sample (Fig. 4), which leads to a lot of background noise from the glass slide used as a sample holder. The shoulders on the low angle side of the peaks of the (001)-oriented single crystal may be caused by a skin layer on the sample [35]. The XRD pattern and Rietveld refinement of the NBT-25SCT polycrystalline sample is shown in Fig. 6. The pattern was refined using mixed rhombohedral (*R3c*) and cubic $\left(Pm\bar{3}m\right)$ phases. The sample consists of 97 vol % rhombohedral and 3 vol % cubic phases.

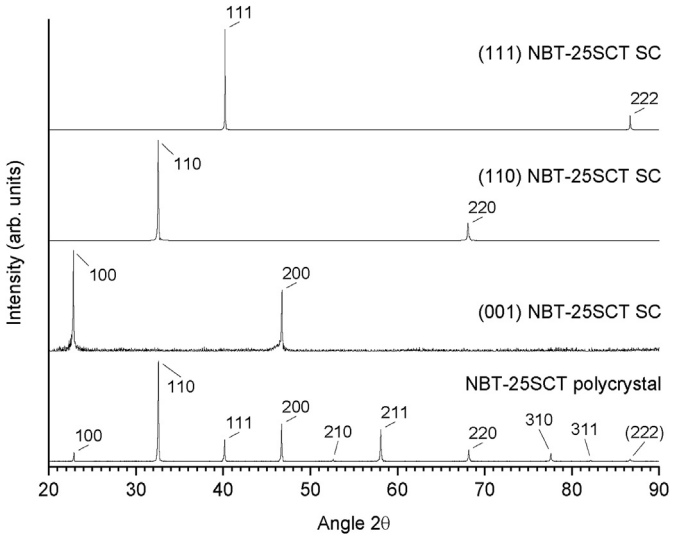


**Fig. 5.** XRD patterns of (001), (110) and (111)-oriented $0.75(Na_{0.5}Bi_{0.5})TiO_3$–$0.25(Sr_{0.7}Ca_{0.3})TiO_3$ single crystals and a polycrystalline sample.

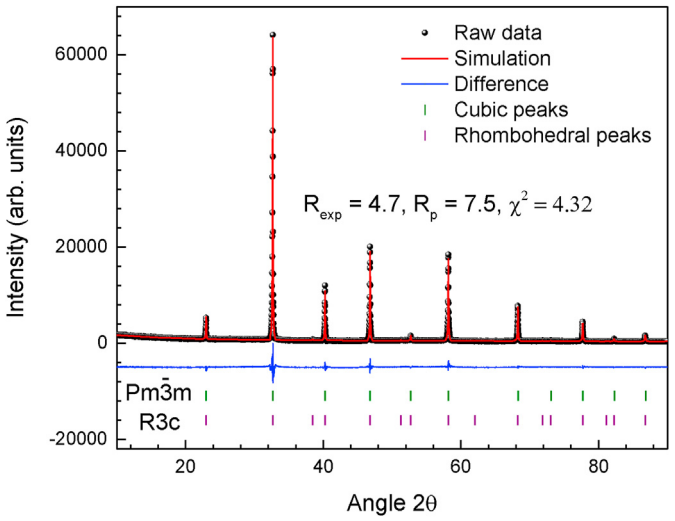


**Fig. 6.** XRD pattern and Rietveld refinement of a polycrystalline $0.75(Na_{0.5}Bi_{0.5})TiO_3$–$0.25(Sr_{0.7}Ca_{0.3})TiO_3$ sample.

A Raman spectrum of an NBT-25SCT single crystal is shown in Fig. 7. Peak fitting of Gaussian peaks is carried out using fityk 0.9.8 peak fitting software [36]. The black curve is the original data, the blue curves are the fitted peaks and the red curve is the sum of the fitted peaks. The spectrum is typical of $(Na_{0.5}Bi_{0.5})TiO_3$-based materials [26,29,30,32,37–42]. Comparing the spectrum with those from the $(Na_{0.5}Bi_{0.5})TiO_3$–$BaTiO_3$ system [40,42] and $(Na_{1-x}K_x)_{0.5}Bi_{0.5}TiO_3$ system [39] indicates the structure to be rhombohedral: the peak at 140 $cm^{-1}$ is sharply defined, the peak at 260 $cm^{-1}$ is narrow and the peaks between 450 and 650 $cm^{-1}$ are merged together.

The polarization vs. electric field and bipolar strain vs. electric field hysteresis loops of the (001), (110) and (111)-oriented NBT-25SCT single crystals for a maximum electric field of 4 kV/mm are shown in Fig. 8. Ferroelectric and piezoelectric properties of the single crystals are given in Table 3. The (001)-oriented NBT-25SCT single crystal has a very slim and unsaturated polarization hysteresis loop, with low values of remanent polarization $P_r$, saturation polarization $P_s$ and coercivity $E_c$. The polarization hysteresis loops of the (110) and (111)-oriented NBT-25SCT single crystals are well saturated and have a pinched appearance. The

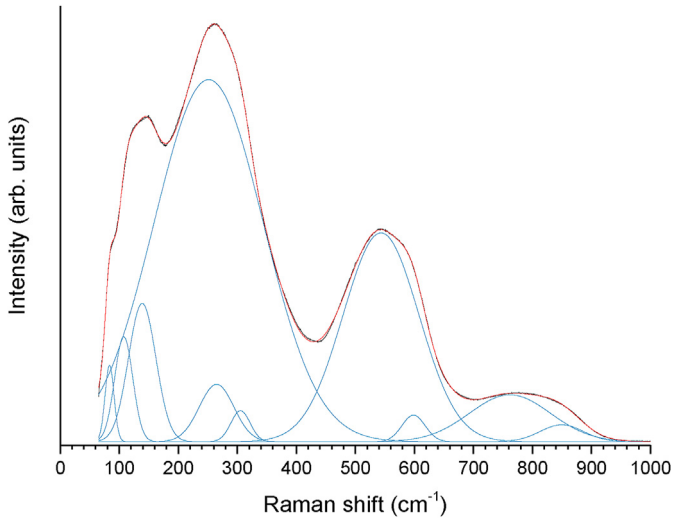


**Fig. 7.** Raman spectrum of a $0.75(Na_{0.5}Bi_{0.5})TiO_3$–$0.25(Sr_{0.7}Ca_{0.3})TiO_3$ single crystal.

upward curvature of the hysteresis loop of the (110)-oriented NBT-25SCT single crystal between $P_s$ and $P_r$ indicates that the material is semiconducting [43]. The (111)-oriented NBT-25SCT single crystal has a slimmer hysteresis loop, with lower values of $P_r$ and $E_c$ compared to the (110)-oriented single crystal, although $P_s$ is higher. This hysteresis loop does not show the upward curvature between $P_s$ and $P_r$, indicating that conductivity is lower in the [111] direction. The bipolar strain hysteresis loop of the (001)-oriented NBT-25SCT single crystal is very slim with low maximum strain $S_{max}$, negative strain $S_{neg}$, strain hysteresis $\Delta S/S_{max}$ (where $\Delta S$ is the difference between the upper and lower values of strain at an electric field of 2 kV/mm) and $d_{33}^*$ (= $S_{max}/E_{max}$). The (110) and (111)-oriented NBT-25SCT single crystals have partially sprout-shaped hysteresis loops with much larger values of $S_{max}$, $S_{neg}$, $\Delta S/S_{max}$ and $d_{33}^*$. The (111)-oriented NBT-25SCT single crystal has the largest values of strain and $d_{33}^*$.

Fig. 9 shows the polarization vs. electric field and bipolar strain vs. electric field hysteresis loops of a (001)-oriented NBT-25SCT single crystal under maximum electric fields of between 4 and 7.5 kV/mm. The corresponding ferroelectric and piezoelectric properties are shown in Table 4. The curves under a maximum electric field of 4 kV/mm are the same as those in Fig. 8. As the electric field increases above 4 kV/mm, the polarization hysteresis loops become more saturated. However, they remain narrower than the loops of the (110) and (111)-oriented NBT-25SCT single crystals and do not have the kinked appearance. The gaps between the beginning and end of the loops indicate that the material is semiconducting [43]. The bipolar strain loops also show increasing values of $S_{max}$ and $d_{33}^*$. For the electric field of 7.5 kV/mm, $d_{33}^*$ exceeds that of the (111)-oriented NBT-25SCT single crystal. Furthermore, the bipolar strain loops remain very slim with low values of strain hysteresis and almost no negative strain. Fig. 9 (c) shows a plot of strain vs. the square of the polarization. The curves are vertically offset for clarity. At a maximum electric field of 4 kV/mm, the curve is almost hysteresis-free, following almost linear behaviour. As the maximum electric field increases hysteresis becomes more apparent.

Plots of the real ($\varepsilon_r$') part of the complex relative permittivity vs. temperature, loss tangent vs. temperature and conductivity vs. temperature of the (001), (110) and (111)-oriented NBT-25SCT single crystals are shown in Fig. 10. The numbers in the legends are the logarithmic values of the measurement frequency. The arrows indicate the direction of increasing frequency. All of the single crystals show relaxor behaviour typical of NBT-type materials [29,30,32,33,44–46]. The plots of $\varepsilon_r$' vs. temperature show broad peaks with a maximum $T_m$ at ~290–300 °C and a shoulder $T_s$ at ~170–180 °C. At temperatures below $T_s$, $\varepsilon_r$' shows

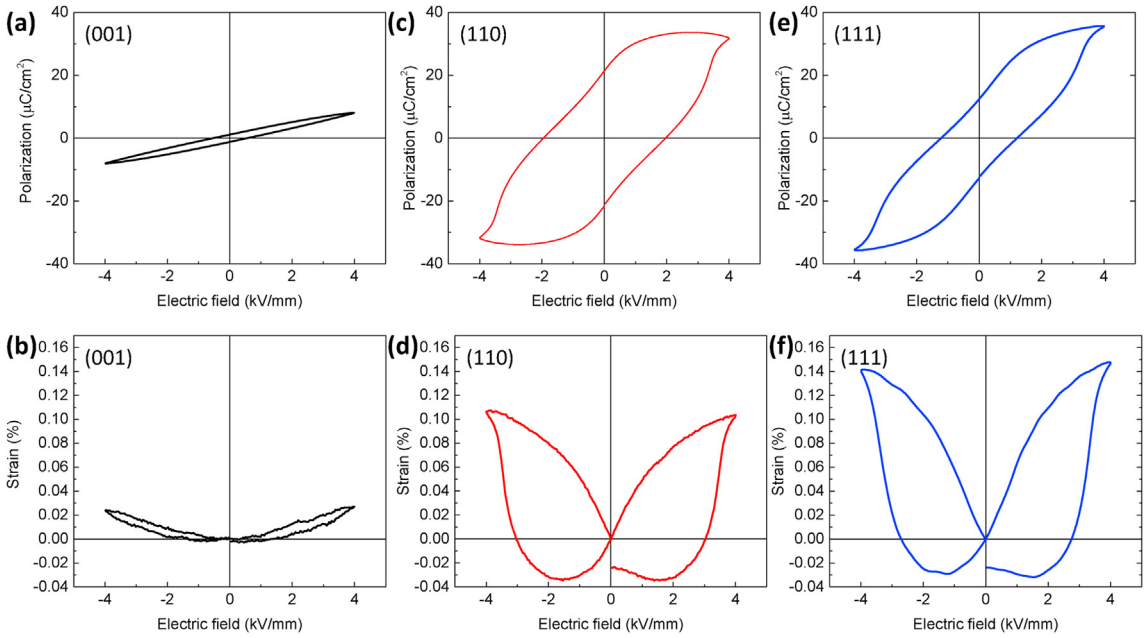


**Fig. 8.** Polarization vs. electric field and bipolar strain vs. electric field hysteresis loops of (a, b) (001), (c, d) (110) and (e, f) (111)-oriented $0.75(Na_{0.5}Bi_{0.5})TiO_3$–$0.25(Sr_{0.7}Ca_{0.3})TiO_3$ single crystals.

**Table 3**
Ferroelectric and Piezoelectric properties of (001), (110) and (111)-oriented $0.75(Na_{0.5}Bi_{0.5})TiO_3$–$0.25(Sr_{0.7}Ca_{0.3})TiO_3$ single crystals under a maximum electric field of 4 kV/mm.

| Orientation | $P_s$ (μC/cm²) | $P_r$ (μC/cm²) | $E_c$ (kV/mm) | $S_{max}$ (%) | $S_{neg}$ (%) | $\Delta S/S_{max}$ | $d_{33}$* (pm/V) |
|---|---|---|---|---|---|---|---|
| (001) | 8.05 | 1.10 | -0.52 | 0.027 | -0.003 | 0.290 | 68 |
| (110) | 31.88 | 24.41 | -1.95 | 0.104 | -0.035 | 1.057 | 259 |
| (111) | 35.61 | 12.50 | -1.22 | 0.148 | -0.032 | 0.918 | 369 |

dispersion with frequency. The values of $T_s$ and $T_m$ are higher than in single crystals of NBT-25ST (~135 and ~190 °C respectively) [30]. The values of $\varepsilon_r$' for the (001)-oriented NBT-25SCT single crystal are slightly higher than those of the (110) and (111)-oriented single crystals. The (111)-oriented NBT-25SCT single crystal exhibits the monotonic frequency dispersion in tan δ in the temperature range 30–300 °C, which is not clear in the (001) and (110)-oriented crystals. The behaviour can be matched with AC conductivity plots in Fig. 10 (c) as $\sigma' = \omega\varepsilon_0\varepsilon_r$". While the (111)-oriented NBT-25SCT single crystal exhibits nearly constant, slightly decreasing $\varepsilon_r$" with decreasing frequency, the (001) and (110)-oriented crystals exhibit increasing $\varepsilon_r$" at lower frequencies, resulting in non-monotonic tan δ.

**Table 4**
Ferroelectric and Piezoelectric properties of a (001)-oriented $0.75(Na_{0.5}Bi_{0.5})TiO_3$–$0.25(Sr_{0.7}Ca_{0.3})TiO_3$ single crystal under a maximum electric field of 4–7.5 kV/mm.

| Electric field (kV/mm) | $P_s$ (μC/cm²) | $P_r$ (μC/cm²) | $E_c$ (kV/mm) | $S_{max}$ (%) | $S_{neg}$ (%) | $\Delta S/S_{max}$ | $d_{33}$* (pm/V) |
|---|---|---|---|---|---|---|---|
| 4 | 8.05 | 1.10 | -0.52 | 0.027 | -0.003 | 0.290 | 68 |
| 6.5 | 18.69 | 3.79 | -1.13 | 0.114 | -0.003 | 0.287 | 176 |
| 7.5 | 22.17 | 4.46 | -1.17 | 0.320 | -0.010 | 0.276 | 429 |

## 4. Discussion

The basis of the solid state crystal growth technique used to grow the NBT-25SCT single crystals has been explained using the mixed control mechanism of microstructure evolution [31,47–49]. According to this mechanism, the growth of the single crystal depends upon both its interfacial structure with the surrounding matrix grains and on the mean matrix grain size. To grow a large single crystal, it is important to restrict grain growth in the matrix, as the driving force for single crystal growth is inversely proportional to the mean matrix grain size. In particular, abnormal grain growth in the matrix must be avoided as the abnormal grains can block the single crystal and prevent it from growing further. Compared with the NBT-25ST single crystal grown by top-seeded solid

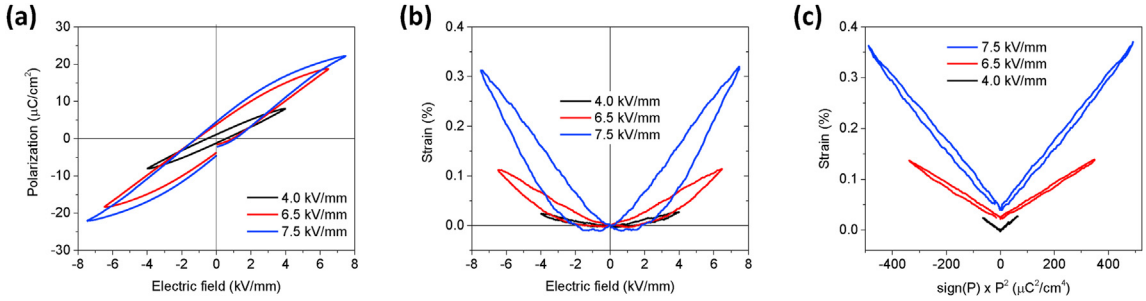


**Fig. 9.** (a) Polarization vs. electric field and (b) bipolar strain vs. electric field hysteresis loops of a (001)-oriented $0.75(Na_{0.5}Bi_{0.5})TiO_3$–$0.25(Sr_{0.7}Ca_{0.3})TiO_3$ single crystal under a maximum electric field of 4–7.5 kV/mm; (c) strain vs. squared polarization.

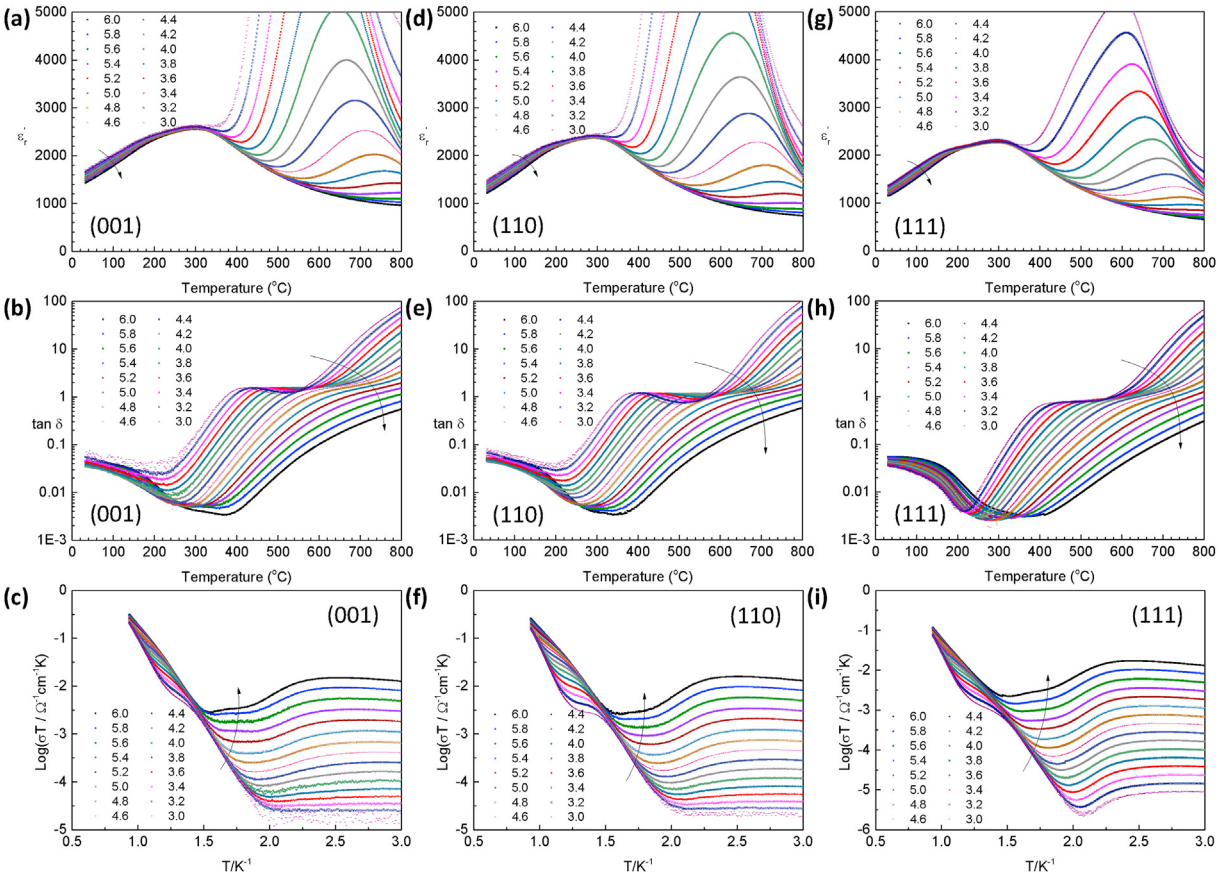


**Fig. 10.** Real part of relative permittivity, loss tangent and conductivity vs. temperature plots of the: (a–c) (001); (d–f) (110) and (g–i) (111)-oriented $0.75(Na_{0.5}Bi_{0.5})TiO_3$–$0.25(Sr_{0.7}Ca_{0.3})TiO_3$ single crystals.

state crystal growth in our previous work, the mean matrix grain size of the NBT-25SCT single crystals grown by top-seeded solid state crystal growth is smaller (10–11 μm vs. 14 μm) [30]. This increases the driving force for single crystal growth, allowing a large NBT-25SCT single crystal to be grown in only 20 h. In the crystal grown by solid state crystal growth, single crystal growth and densification of the matrix take place simultaneously. If the single crystal/matrix grain boundary is moving too quickly, then pores on the boundary may become trapped in the single crystal [50]. Therefore many pores in the matrix were trapped inside the growing single crystal as a result of the incomplete densification process (Fig. 3). In the case of top-seeded solid state crystal growth, pre-sintering the pellet allowed partial densification, reducing the number of pores available for the single crystal to absorb during growth.

Relaxor ferroelectric behaviour is encountered in both lead-based and lead-free ferroelectric materials [3,51,52] and is commonly observed in $(Na_{0.5}Bi_{0.5})TiO_3$-based compositions [8,32,44,53–55]. Numerous theories were constructed to interpret relaxor behaviour such as the space charge model, diffuse phase transition model, dipolar glass model and random field model. The existence of polar nanoregions (PNRs), nanometer-sized regions in which polarization is correlated, is believed to be the reason for the dielectric relaxation behaviour in relaxor materials [3,51,52,56]. The reorientation of the PNRs' dipole moments in an alternating electric field as functions of temperature and frequency determines the dielectric relaxation behaviour of these materials. PNRs form at (or possibly above) the Burns temperature $T_B$ above $T_m$ [57,58]. At this temperature, the dipole moments of the PNRs have sufficient thermal energy to fluctuate between different directions and can reorient in response to an electric field, returning to a low free energy state after the field disappears. As the temperature decreases, the PNRs grow larger and increasingly interact with each other, slowing down their response to the electric field. A range of PNRs with different sizes and relaxation times causes the broad peak of relative permittivity vs. temperature. Eventually, when the temperature goes down to the freezing temperature $T_f$, the relaxation time of the PNRs becomes very long and their dipole moments can no longer reorient in the electric field. In $(Na_{0.5}Bi_{0.5})TiO_3$-based compositions there is often also a low temperature shoulder ($T_s$) in the relative permittivity vs. temperature plots. This shoulder has been ascribed to several possible phenomena including a transition from the rhombohedral phase to mixed rhombohedral and tetragonal phases [13,23,59–61], thermal evolution of mixed rhombohedral and tetragonal polar nanoregions [62], a transition from a non-ergodic to ergodic relaxor [63] or from a ferroelectric to a relaxor state [64].

Although it has been studied for over 50 years, the nature of the room temperature $(Na_{0.5}Bi_{0.5})TiO_3$ structure is still contentious and different structures have been perceived according to different measurement techniques [65,66]. Firstly, based on X-ray diffraction $(Na_{0.5}Bi_{0.5})TiO_3$ was determined to have a pseudocubic [67,68] or rhombohedral structure with *R3c* or *R3m* space group [59,69]. Neutron diffraction studies also indicated the *R3c* structure [59]. Transmission Electron Microscopy studies indicated coexisting rhombohedral (*R3c*) and tetragonal (*P4bm* or $P4_2nm$) phases [70]. More recently, relying on high resolution X-ray diffraction, the monoclinic *Cc* space group, with a slight deviation from rhombohedral symmetry, was proposed [66]. This proposal of a monoclinic unit cell was further supported by optical studies [71]. However, even the assignment of the monoclinic *Cc* space group cannot explain all the features of the $(Na_{0.5}Bi_{0.5})TiO_3$ structure and the room temperature phase may be a combination of *R3c* and *Cc* phases [72,73]. There is also considerable local chemical and structural disorder in $(Na_{0.5}Bi_{0.5})TiO_3$, which can cause deviations from the average structures measured by XRD, neutron diffraction and TEM. The shortest Bi–O bond length for

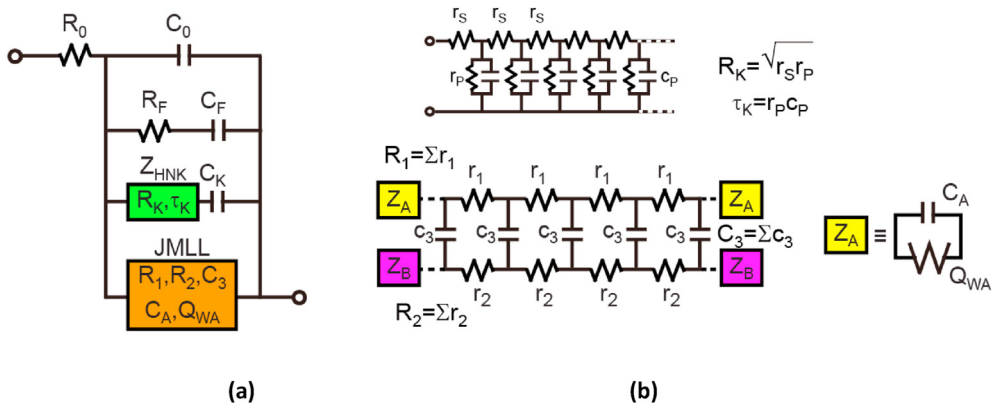


**Fig. 11.** Equivalent circuit modelling of the AC response of $0.75(Na_{0.5}Bi_{0.5})TiO_3$–$0.25(Sr_{0.7}Ca_{0.3})TiO_3$ single crystals by twelve parameters.(a). $Z_{HNK}$ and JMLL are transmission line models (b).

$(Na_{0.5}Bi_{0.5})TiO_3$ was found to be 2.22 Å by X-ray absorption fine structure (XAFS) measurements, which is shorter than the values measured from neutron diffraction [74]. This means that Bi is displaced from the centre of its oxygen polyhedron forming short bonds with several oxygen atoms. Ti displacement was found to be larger and Bi–Ti distances were found to be shorter than expected from neutron diffraction experiments. Using nuclear magnetic resonance (NMR), significant disorder was found for the local structure of sodium, which was attributed to a unimodal distribution of octahedral tilting as opposed to two coexisting tilt systems such as $a^-a^-a^-$ and $a^-a^-c^+$ previously reported for $(Na_{0.5}Bi_{0.5})TiO_3$ [75,76]. A summary of the complexities of the $(Na_{0.5}Bi_{0.5})TiO_3$ structure is given by Paterson et al. [55].

Based on the Rietveld refinement of the XRD pattern of a polycrystalline sample, NBT-25SCT contains coexisting rhombohedral *R3c* and cubic $\left(Pm\bar{3}m\right)$ phases, as was previously found for the base NBT-25ST composition [30]. This is as expected as the NBT-25ST composition lies on or near the MPB between rhombohedral and tetragonal/-pseudocubic phases [7,77,78]. Compared with the NBT-25ST composition, NBT-25SCT contains a higher proportion of rhombohedral phase (97 vol % vs. 76 vol %). This agrees with earlier work in the $0.8(Na_{0.5}Bi_{0.5})TiO_3$-$0.2(Sr_{1-x}Ca_x)TiO_3$ system, where substitution of Ca for Sr increased the amount of rhombohedral phase [33]. Compared with the NBT-25ST single crystal, the Raman scattering spectrum of the NBT-25SCT single crystal shows that the unit cell is predominantly rhombohedral (Fig. 7). The peak at 140 $cm^{-1}$ is more prominent for the NBT-25SCT single crystal, the peak at 260 $cm^{-1}$ is narrower and the peaks between 450 and 650 $cm^{-1}$ are more strongly merged together. The Goldschmidt tolerance factor (using an ionic radius of 0.135 nm for $Bi^{3+}$ with coordination number = 12 [79]) was calculated to decrease from 0.981 (NBT-25ST) to 0.978 (NBT-25SCT), due to the smaller ionic radius of Ca compared to Sr (0.134 nm vs. 0.144 nm for coordination number = 12) [80]. The decrease in tolerance factor will promote octahedral tilting and rotation [81], which should lead to an increased rhombohedral distortion compared to NBT-25ST, as seen in the XRD and Raman scattering results. Hiruma et al. found that the MPB composition for $(Na_{0.5}Bi_{0.5})TiO_3$-based solid solutions appears for tolerance factors between 0.982 and 0.986 [54,79]. Similar results were found by Bai et al. for ternary systems [82–84]. Hence the decreased tolerance factor for NBT-25SCT moves it further from the MPB composition into the rhombohedral phase field of the $(Na_{0.5}Bi_{0.5})TiO_3$–$SrTiO_3$ phase diagram.

As was previously found for the $0.8(Na_{0.5}Bi_{0.5})TiO_3$-$0.2(Sr_{1-x}Ca_x)TiO_3$ system, substitution of Ca for Sr increases both $T_s$ and $T_m$ compared to the base NBT-25ST composition (Fig. 10) [33]. Assuming that $T_s$ corresponds to the rhombohedral-tetragonal transition temperature [7,13,23,44,54,59–61], its increase is caused by the increased stabilisation of the rhombohedral phase in NBT-25SCT. The increase in $T_s$ is the probable cause of the reduction in the inverse piezoelectric performance (Fig. 9 and Table 3) compared to the base NBT-25ST composition. Many researchers have noted that the best inverse piezoelectric performance is found when $T_s \approx$ room temperature [7,18,44,54,79,83–85]. Replacing Sr with Ca reduces the tolerance factor of the solid solution end member from 0.999 for $SrTiO_3$ to 0.989 for $(Sr_{0.7}Ca_{0.3})TiO_3$. This may cause the MPB composition to shift to lower $(Na_{0.5}Bi_{0.5})TiO_3$ content and $T_s$ to increase [54,79,82].

In the NBT-25ST single crystals, the [001] direction was found to have the best inverse piezoelectric properties [30]. However, for the NBT-25SCT single crystal the [111] direction has the best inverse piezoelectric properties (Fig. 8 and Table 3). This change may also be related to the increased amount of rhombohedral phase in the NBT-25SCT single crystal. Schneider et al. found that $(Na_{0.5}Bi_{0.5})TiO_3$-3.6 mol % $BaTiO_3$ single crystals, which are in the rhombohedral *R3c* phase field of the $(Na_{0.5}Bi_{0.5})TiO_3$–$BaTiO_3$ phase diagram, had highest $S_{max}$ and $S_{neg}$ in the <111> direction, followed by the <110> direction, whereas the crystal oriented in the <001> direction had low values of $S_{max}$ and $S_{neg}$ [86]. Similar behaviour is found in the NBT-25SCT single crystals. For single crystals of $(Na_{0.5}Bi_{0.5})TiO_3$–$BaTiO_3$ with higher $BaTiO_3$ (and hence tetragonal phase) content, the direction of highest $S_{max}$ switched to <001> [85,86], as was the case for the NBT-25ST single crystals.

The NBT-25SCT single crystals oriented in the [110] and [111] directions have pinched polarization hysteresis loops, which indicates that an electric field-induced phase transition is taking place [87]. However, the corresponding bipolar strain hysteresis loops have a noticeable negative strain and lack the "sprout shape" associated with the electric field-induced phase transition [87]. This implies that the long-range ferroelectric ordering of $(Na_{0.5}Bi_{0.5})TiO_3$ that is induced by the applied electric field [88,89] is partially disturbed by the incorporation of $(Sr_{0.7}Ca_{0.3})TiO_3$, but that a polar phase remains when the electric field returns to zero [87,90]. The strain behaviour of the NBT-25SCT single crystal oriented in the [001] direction is predominantly electrostrictive at an electric field of 4 kV/mm [Fig. 9 (c)]. As electric field increases, the behaviour changes from electrostrictive to ferroelectric/piezoelectric, as shown by the broadening polarization and strain hysteresis loops, and the broadening of the strain vs. polarization squared loops [91]. This indicates that the applied electric field is inducing a long-range ferroelectric ordering.

Temperature dependent AC responses in Fig. 10 should represent the dielectric and conduction properties in relation with the phases, microstructures and crystallographic orientations. Indeed interesting frequency-temperature variations can be noted in the raw AC data in different representations. Any definite description can be made only by physics-based parameterisation or equivalent circuit modelling, which has not been reported so far. In this work, a preliminary but promising physics-based modelling analysis is performed. The equivalent circuit

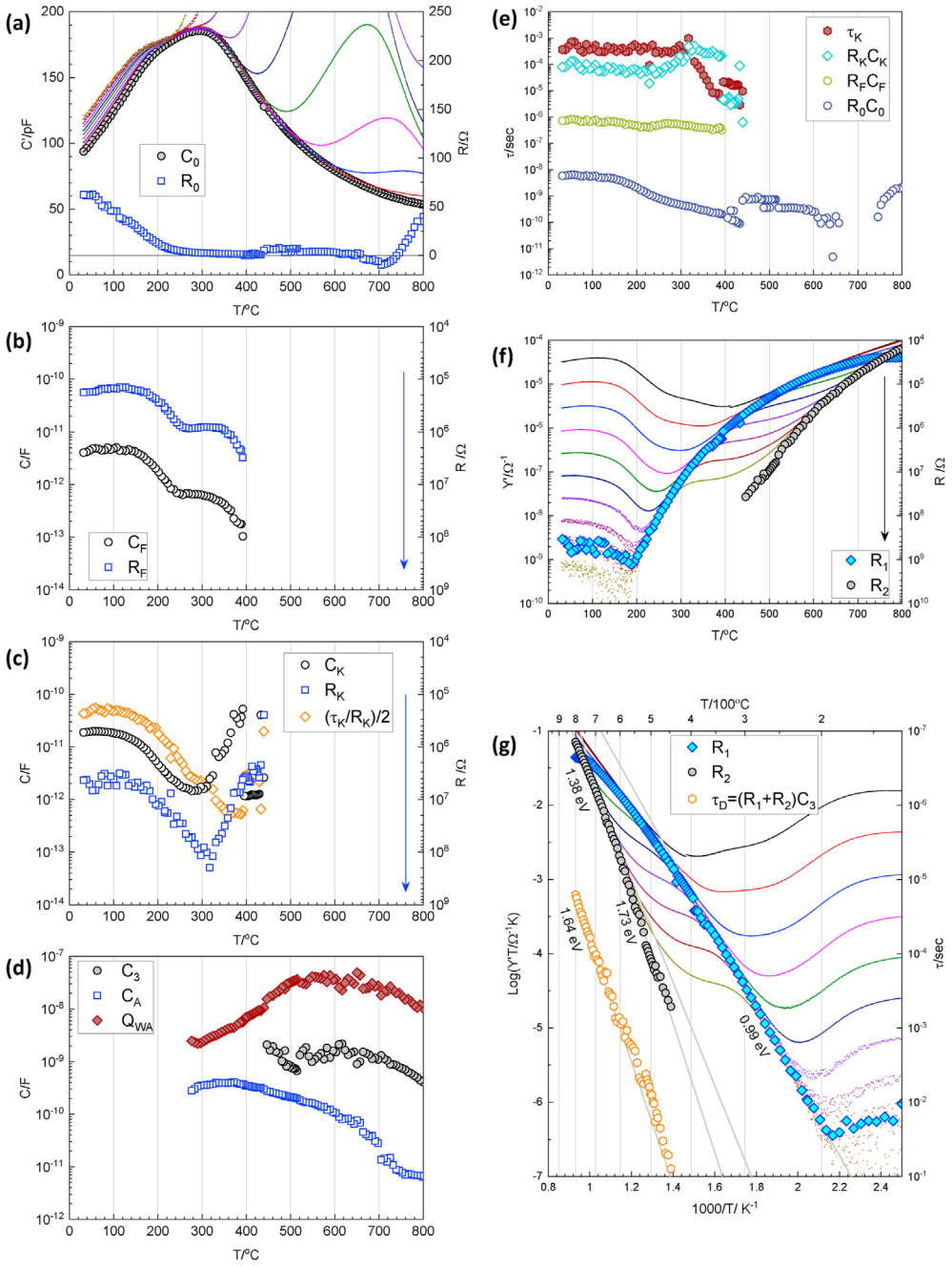


**Fig. 12.** Twelve modelling parameters compared with the raw AC data in various presentations for the data of the (111)-oriented $0.75(Na_{0.5}Bi_{0.5})TiO_3$–$0.25(Sr_{0.7}Ca_{0.3})TiO_3$ single crystal. Derived capacitances and time constants are also shown.

parameters are twelve as schematically represented in Fig. 11: $R_0$, $C_0$, $R_F$, $C_F$, $R_K$, $\tau_K$, $C_K$, $R_1$, $R_2$, $C_3$, $C_A$ and $R_{WA}$. $R_0$, $C_0$ and $R_1$ parameters are used for the whole temperature range. The modelled response may not be visible due to the frequency limit but may be characteristic of the sample state at different temperature ranges. Fitting of the series of data can be best made by gradually changing model parameters from the high temperature to the low temperature. Model parameters used at different temperatures can be seen in the graphs of Fig. 12. Unlike Fig. 10 the data are not normalized with the geometry factor i.e. area/thickness ratio. Sample geometry should be properly considered for the respective model parameters. Interfacial components should be normalized with respect to area, and chemical capacitance, and probably also $C_K$, are proportional to the sample volume. The parameters of the different samples are compared with geometry factors as in Table 2. While $C_0$ and $R_2$ can be normalized with respect to area/thickness ratio, there is no clear geometry correlation in the $C_A$, $Q_{WA}$, $C_K$, $C_F$, $R_K$, $R_F$, and $R_1$ parameters.

A frequency-independent ideal capacitance $C_0$ for the relative permittivity can be modelled for all temperature ranges, which coincide with the highest frequency capacitance curves at low temperature but are extrapolated at high temperature by fitting analysis, Fig. 12 (a). Note that the relative permittivity $\varepsilon_r$' is now unambiguously defined from $C_0$, as $C_0$ is a frequency independent parameter. The residual series resistance, $R_0$, is critical in the present model analysis imposing well-defined impedance functions with the characteristic high frequency limiting behavior, Fig. 11. At low temperature $R_0$ or $R_0C_0$ Fig. 12 (e) indicates the behavior of tan δ, suggesting its origin. For the high temperature response with large low frequency polarization and two thermally activated conduction processes, a mixed conduction modelling is made using JMLL (Jamnik-

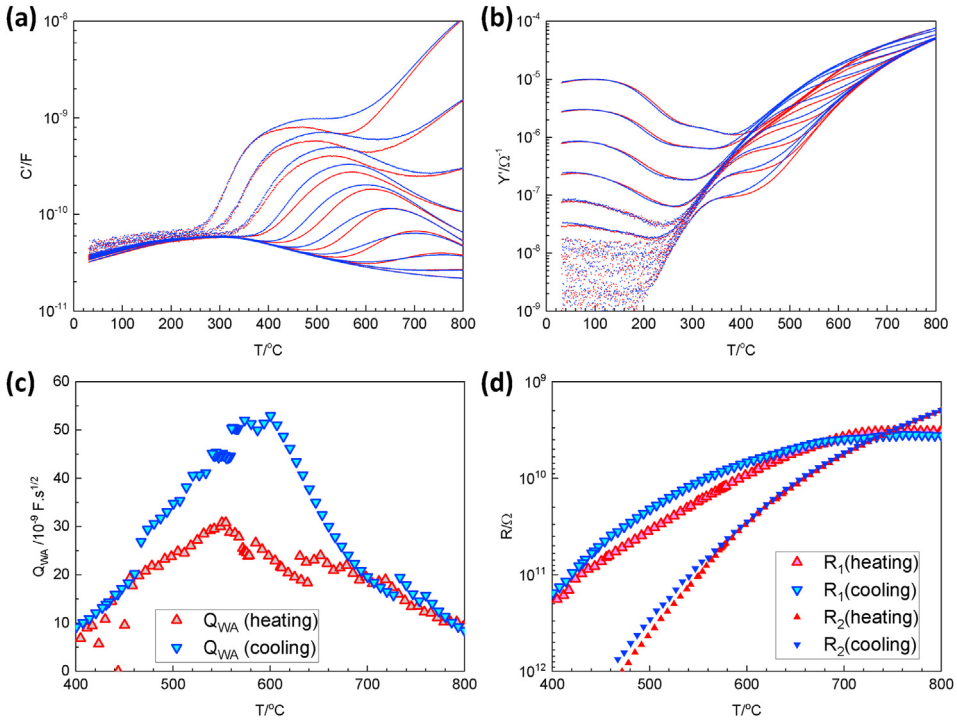


**Fig. 13.** Thermal hysteresis in (a) capacitance and (b) admittance behaviour of the (001) oriented $0.75(Na_{0.5}Bi_{0.5})TiO_3$–$0.25(Sr_{0.7}Ca_{0.3})TiO_3$ single crystal, which are represented by the $Q_{WA}$ and $R_1$ parameters.

Maier-Lai-Lee) models implemented in commercial impedance analysis software, ZView (Scribner Ass. Inc., Southern Pines, NC). Two overlapped impedance arcs shown in the high temperature data (Fig. S1) cannot be attributed to the grain boundary blocking effects [92], as the samples are nominally single crystalline. Rather a mixed conductor model may be applicable [93], as an oxide ion conduction mechanism is suggested in acceptor-doped NBT systems [94]. In contrast to conventional brick-layer modelling which separates two resistance components in series, mixed conductor modelling considers two resistance components for ionic and electronic conduction in parallel, which are $R_1$ and $R_2$, respectively, and the ionic conduction may be assumed to be selectively blocked at the electrodes. The blocking effect is here ingeniously represented by an ideal capacitance $C_A$ and also a Warburg impedance $Q_{WA}$ in parallel. The latter has been a generic feature for many electrochemical systems explaining the low frequency polarizations without resorting to CPE (constant phase element) modelling with arbitrarily adjusted frequency dispersions [92,95–97]. For the high temperature data above 700 °C, the low frequency polarization can be modelled by the terminal impedance $Z_B$. As the observations are rather limited, for the analysis of such high temperature data, the low frequency range is not included (See Fig. S1).

Temperature dependence of $R_1$ and $R_2$ components, indicated in Fig. 12 (g), also matches with the values reported for ionic and electronic conductivities [94]. Large polarization around 500 °C is shown to be described by the $Q_{WA}$ parameter. (Another increase at higher temperature is caused by the $Z_B$ component, which is not modelled.) In the repeated and continuous slow heating and cooling cycling in the electrical measurements, well-behaved hysteresis is observed above $T_m$ for (001) and (110) oriented crystals as shown in Fig. 13. The hysteresis can be mainly attributed to $Q_{WA}$ and $R_1$ parameters, which represents the ionic conduction and the diffusion effects. Hysteresis in the similar perovskite oxides at high temperature transitions are characteristic of ferro-paraelastic transitions and the present analysis shows the hysteresis in the transition is associated with the ionic defect formation. For the same measurement schedules the hysteresis is not observed for the (111)-oriented crystal and the transitions are more strongly indicated. This may be related to the good inverse piezoelectric properties of the (111)-oriented sample as discussed above (Fig. 8 and Table 3). The parameter $R_1$ is modelled throughout the temperature range and represents the trace shown by AC conductivity curves, Fig. 12 (g). Related electrode parameters $C_A$ and $Q_{WA}$ can be evaluated down to around 300 °C. The parameter $R_2$ coincides with the overlapped traces of AC conductivity curves. Because of the limited visibility with lowering temperature, the Arrhenius behavior appears to stop around 420 °C and the resistance becomes very large. With infinitely large $R_2$ or open terminal below this transition, all other parameters can be consistently evaluated. Chemical capacitance $C_3$ can be modelled together with $R_1$. This parameter may represent the electronic carrier concentration, which is considered a minority in number compared to the large number of ionic defects but thermally activated defect formation is not indicated, which needs further study. Diffusion relaxation time according to the mixed conductor model is also indicated in Fig. 12 (g).

Below the characteristic temperature where the response represented by $R_2$ and $C_3$ disappear, ~430 °C, $R_1$ and the associated electrode parameter can be simply modelled in a series circuit, Fig. S2. Now more visible frequency dispersion is modelled as a series connection of a Havriliak-Negami impedance, $Z_{HNK}$ and a capacitance $C_K$, a modified Debye model. Previously, Havriliak-Negami capacitance functions [95, 98] were suggested to describe the apparent dielectric effects from the mobile charge carriers, as an approximation of the CK model, originally suggested by MacDonald [95,99]. After testing different impedance function and frequency exponents, presently, a Havriliak-Negami impedance with exponents ½ and 1 was found satisfactory. This particular Havarililak-Negami impedance is also represented as a Gerischer impedance, illustrated in Fig. 11 (b). As shown in Fig. 12 (c) and (e), $R_K$ and $C_K$ shows the characteristic transition at slightly over 300 °C in the way that the $R_KC_K$ product becomes less temperature dependent. Model parameter $\tau_K$ and the $R_KC_K$ product are more distinguished for the (111) crystal data, compared to the situation for the (110) and (001) oriented crystals, Fig. 14. The difference in the frequency dispersion of tan δ between the (111) crystal and the other crystals below ~250 °C appears to be indicated in the well-behaved $\tau_K$ and $R_KC_K$ parameters of the (111)

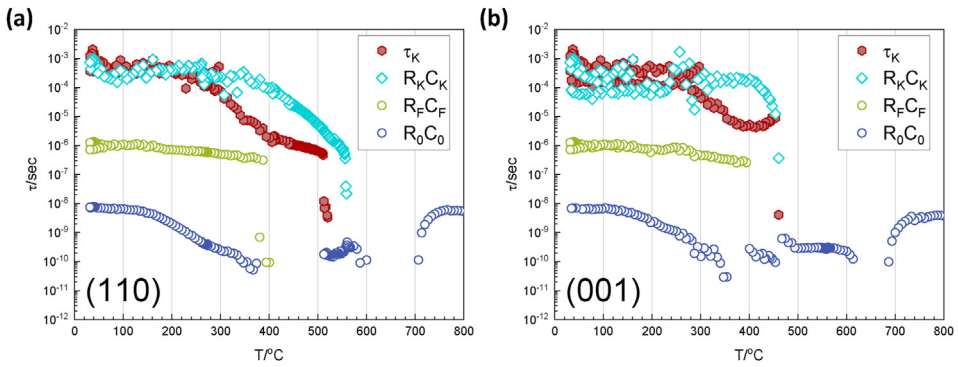


**Fig. 14.** Time constants from impedance analysis of the (110) and (001) oriented 0.75($Na_{0.5}Bi_{0.5}$)$TiO_3$–0.25($Sr_{0.7}Ca_{0.3}$)$TiO_3$ single crystals, which can be compared to those of the (111)-oriented crystal in Fig. 12(e).

crystal. Below 400 °C a well-behaved Debye circuit $R_F$ and $C_F$ is needed, which shows a characteristic temperature dependence as shown in Fig. 12 (b), similar to the tan δ curves. The product $R_FC_F$ is around $10^{-6}$ s for all samples.

The superior description of the dispersed impedance of solid electrolytes as additive capacitance effects has been reported [92,95,99] for the apparent dielectric polarization of mobile charge carriers, including grain boundary blocking effects. The mixed conduction model is also based on the parallel network of two resistors and the effective parallel connected capacitance effects. A capacitance-focused parallel network is generally more physics-based. Not only by the parameter values or temperature dependences, but also the appearance/disappearance of the partial model responses appear to indicate the phase or ordering/interaction transition points.

## 5. Conclusions

In this work, single crystals of 0.75($Na_{0.5}Bi_{0.5}$)$TiO_3$-0.25($Sr_{0.7}Ca_{0.3}$)$TiO_3$ of (001), (110) and (111) orientation were fabricated successfully by the top-seeded solid state crystal growth technique. Replacement of Sr with Ca restricts matrix grain growth compared to the base 0.75($Na_{0.5}Bi_{0.5}$)$TiO_3$-0.25$SrTiO_3$ composition, increasing the driving force for single crystal growth and promoting single crystal growth. Use of pre-sintered substrates resulted in an increase in single crystal density, as compared to the solid state crystal growth technique. The structure of the 0.75($Na_{0.5}Bi_{0.5}$)$TiO_3$-0.25($Sr_{0.7}Ca_{0.3}$)$TiO_3$ single crystals is predominantly rhombohedral. Impedance spectroscopy showed that the single crystals show relaxor ferroelectric behaviour typical of ($Na_{0.5}Bi_{0.5}$)$TiO_3$-type materials, and that Ca substitution for Sr causes an increase in the shoulder temperature $T_s$ and the temperature of maximum relative permittivity $T_m$. Polarization and bipolar strain versus electric field loops showed ferroelectricity and piezoelectricity in (110)- and (111)-oriented single crystals, whereas (001)-oriented single crystals initially show electrostrictive behaviour, followed by ferroelectric/piezoelectric behaviour with increasing electric field. Compared to the base 0.75($Na_{0.5}Bi_{0.5}$)$TiO_3$-0.25$SrTiO_3$ composition, the orientation with the highest value of $d_{33}$* changed from (001) to (111) for the 0.75($Na_{0.5}Bi_{0.5}$)$TiO_3$-0.25($Sr_{0.7}Ca_{0.3}$)$TiO_3$ composition. A full parametric impedance modelling over the wide temperature range is successfully performed by taking the mixed ionic and electronic conduction as well as universal dielectric response behaviour. The fitted parameters are shown to represent the features of the raw data, which allows the identification of the transition points and the associated processes. The impedance parameters appear to be related to the piezoelectric performance.

## Declaration of competing interest

The authors declare that they have no known competing financial interests or personal relationships that could have appeared to influence the work reported in this paper.

## Acknowledgements

This research was supported by the Basic Science Research Program through the National Research Foundation of Korea (NRF), funded by the Ministry of Education under Grant numbers 2015R1D1A1A01057060 and 2018R1D1A1B07041485. Jong-Sook Lee acknowledges the support of the National Research Foundation (NRF) of Korea funded by the Ministry of Science and ICT (MSIT) (NRF-2018R1A5A1025224). The authors would like to thank Kyeong-Kap Jeong and Jeong-Yeol Park (Chonnam Centre for Research Facilities, Chonnam National University) for operating the XRD and EPMA, Hey-Jeong Kim (Centre for Development of Fine Chemicals, Chonnam National University) for operating the SEM, and Dr. Sang-Hun Jeong (Korea Basic Science Institute, Gwangju centre) for carrying out the Raman scattering experiment.

## Appendix A. Supplementary data

Supplementary data to this article can be found online at https://doi.org/10.1016/j.oceram.2021.100099.

## References

[1] J. Rödel, W. Jo, K.T.P. Seifert, E.-M. Anton, T. Granzow, D. Damjanovic, Perspective on the development of lead-free piezoceramics, J. Am. Ceram. Soc. 92 (6) (2009) 1153–1177.
[2] D. Damjanovic, N. Klein, J. Li, V. Porokhonskyy, What can be expected from lead-free piezoelectric materials? Funct. Mater. Lett. 3 (1) (2010) 5–13.
[3] V.V. Shvartsman, D.C. Lupascu, Lead-free relaxor ferroelectrics, J. Am. Ceram. Soc. 95 (1) (2012) 1–26.
[4] H.P. Kim, C.W. Ahn, Y. Hwang, H.Y. Lee, W. Jo, Strategies of A Potential importance, making lead-free piezoceramics truly alternative to PZTs, J. Kor. Ceram. Soc. 54 (2) (2017) 86–95.
[5] J. Koruza, A.J. Bell, T. Frömling, K.G. Webber, K. Wang, J. Rödel, Requirements for the transfer of lead-free piezoceramics into application, J. Materiomics 4 (1) (2018) 13–26.
[6] J. Rödel, J.-F. Li, Lead-free piezoceramics: status and perspectives, MRS Bull. 43 (8) (2018) 576–580.
[7] Y. Hiruma, Y. Imai, Y. Watanabe, H. Nagata, T. Takenaka, Large electrostrain near the phase transition temperature of ($Bi_{0.5}Na_{0.5}$)$TiO_3$–$SrTiO_3$ ferroelectric ceramics, Appl. Phys. Lett. 92 (26) (2008) 262904.
[8] M. Acosta, W. Jo, J. Rödel, Temperature- and frequency-dependent properties of the 0.75$Bi_{1/2}Na_{1/2}TiO_3$-0.25$SrTiO_3$ lead-free incipient piezoceramic, J. Am. Ceram. Soc. 97 (6) (2014) 1937–1943.
[9] H.-L. Li, Q. Liu, J.-J. Zhou, K. Wang, J.-F. Li, H. Liu, J.-Z. Fang, Grain size dependent electrostrain in $Bi_{1/2}Na_{1/2}TiO_3$-$SrTiO_3$ incipient piezoceramics, J. Eur. Ceram. Soc. 36 (11) (2016) 2849–2853.
[10] X.-Y. Tong, J.-J. Zhou, K. Wang, H. Liu, J.-Z. Fang, Low-temperature sintered $Bi_{0.5}Na_{0.5}TiO_3$-$SrTiO_3$ incipient piezoceramics and the co-fired multilayer piezoactuator thereof, J. Eur. Ceram. Soc. 37 (15) (2017) 4617–4623.
[11] S. Jo, C.H. Hong, D.S. Kim, H.W. Kang, C.W. Ahn, H.G. Lee, S. Nahm, W. Jo, S.H. Han, Phase transition behavior and mechanical properties of (1-x)($Bi_{1/2}Na_{1/2}$)$TiO_3$-x$SrTiO_3$ lead-free piezoelectric ceramics, Sensor Actuator Phys. 258 (2017) 201–207.

[12] T.A. Duong, H.-S. Han, Y.-H. Hong, Y.-S. Park, H.T.K. Nguyen, T.H. Dinh, J.-S. Lee, Dielectric and piezoelectric properties of $Bi_{1/2}Na_{1/2}TiO_3$–$SrTiO_3$ lead–free ceramics, J. Electroceram. 41 (1) (2018) 73–79.

[13] G. Liu, J. Dong, L. Zhang, Y. Yan, R. Jing, L. Jin, Phase evolution in $(1-x)(Na_{0.5}Bi_{0.5})TiO_3$-$xSrTiO_3$ solid solutions: a study focusing on dielectric and ferroelectric characteristics, J. Materiomics 6 (4) (2020) 677–691.

[14] F. Wang, C. Jin, Q. Yao, W. Shi, Large electrostrictive effect in ternary $Bi_{0.5}Na_{0.5}TiO_3$-based solid solutions, J. Appl. Phys. 114 (2) (2013), 027004.

[15] M. Acosta, L.A. Schmitt, L. Molina-Luna, M.C. Scherrer, M. Brilz, K.G. Webber, M. Deluca, H.J. Kleebe, J. Rödel, W. Donner, Core–Shell lead–free piezoelectric ceramics: current status and advanced characterization of the $Bi_{1/2}Na_{1/2}TiO_3$–$SrTiO_3$ system, J. Am. Ceram. Soc. 98 (11) (2015) 3405–3422.

[16] S. Praharaj, D. Rout, S.J.L. Kang, I.W. Kim, Large electric field induced strain in a new lead-free ternary $Na_{0.5}Bi_{0.5}TiO_3$-$SrTiO_3$-$BaTiO_3$ solid solution, Mater. Lett. 184 (2016) 197–199.

[17] J.H. Cho, J.S. Park, S.W. Kim, Y.H. Jeong, J.S. Yun, W.I. Park, Y.W. Hong, J.H. Paik, Ferroelectric properties and core shell domain structures of Fe-modified $0.77Bi_{0.5}Na_{0.5}TiO_3$-$0.23SrTiO_3$ ceramics, J. Eur. Ceram. Soc. 37 (10) (2017) 3313–3318.

[18] X. Liu, J. Zhai, B. Shen, F. Li, Y. Zhang, P. Li, B. Liu, Electric-field-temperature phase diagram and electromechanical properties in lead-free $(Na_{0.5}Bi_{0.5})TiO_3$-based incipient piezoelectric ceramics, J. Eur. Ceram. Soc. 37 (4) (2017) 1437–1447.

[19] T. Fromling, S. Steiner, A. Ayrikyan, D. Bremecker, M. Durrschnabel, L. Molina-Luna, H.-J. Kleebe, H. Hutter, K.G. Webber, M. Acosta, Designing properties of $(Na_{1/2}Bi_x)TiO_3$-based materials through A-site non-stoichiometry, J. Mater. Chem. C 6 (4) (2018) 738–744.

[20] X. Liu, B. Shen, J. Zhai, Designing novel sodium bismuth titanate lead-free incipient perovskite for piezoactuator applications, J. Am. Ceram. Soc. 102 (11) (2019) 6751–6759.

[21] R.A. Malik, J.-K. Kang, A. Hussain, C.-W. Ahn, H.-S. Han, J.-S. Lee, High strain in lead-free Nb-doped $Bi_{1/2}(Na_{0.84}K_{0.16})_{1/2}TiO_3$–$SrTiO_3$ incipient piezoelectric ceramics, Appl. Phys. Express 7 (6) (2014), 061502.

[22] J.-H. Park, S.-J.L. Kang, Solid-state conversion of $(94-x)(Na_{1/2}Bi_{1/2})TiO_3$-$6BaTiO_3$-$x(K_{1/2}Na_{1/2})NbO_3$ single crystals and their enhanced converse piezoelectric properties, AIP Adv. 6 (1) (2016), 015310.

[23] W. Ge, C. Luo, Q. Zhang, C.P. Devreugd, Y. Ren, J. Li, H. Luo, D. Viehland, Ultrahigh electromechanical response in $(1-x)(Na_{0.5}Bi_{0.5})TiO_3$-$xBaTiO_3$ single-crystals via polarization extension, J. Appl. Phys. 111 (9) (2012), 093508.

[24] Q. Zhang, Y. Zhang, F. Wang, Y. Wang, D. Lin, X. Zhao, H. Luo, W. Ge, D. Viehland, Enhanced piezoelectric and ferroelectric properties in Mn-doped $Na_{0.5}Bi_{0.5}TiO_3$–$BaTiO_3$ single crystals, Appl. Phys. Lett. 95 (10) (2009) 102904.

[25] H. Zhang, H. Deng, C. Chen, L. Li, D. Lin, X. Li, X. Zhao, H. Luo, J. Yan, Chemical nature of giant strain in Mn-doped $0.94(Na_{0.5}Bi_{0.5})TiO_3$–$0.06BaTiO_3$ lead-free ferroelectric single crystals, Scripta Mater. 75 (2014) 50–53.

[26] C. Chen, Y. Wang, X. Jiang, N. Tu, Y. Chen, S. Zhou, X. Xia, Z. Shen, H. Luo, Orientation dependence of electric field induced phase transitions in lead-free $(Na_{0.5}Bi_{0.5})TiO_3$-based single crystals, J. Am. Ceram. Soc. 102 (7) (2019) 4306–4313.

[27] P.G. Le, J.G. Fisher, W.-J. Moon, Effect of composition on the growth of single crystals of $(1-x)(Na_{1/2}Bi_{1/2})TiO_3$-$xSrTiO_3$ by solid state crystal growth, Materials 12 (15) (2019) 2357.

[28] P.G. Le, G.Y. Jo, S.Y. Ko, J.G. Fisher, The effect of sintering temperature and time on the growth of single crystals of 0.75 $(Na_{0.5}Bi_{0.5})TiO_3$–0.25 $SrTiO_3$ by solid state crystal growth, J. Electroceram. 40 (2) (2018) 122–137.

[29] D. Lee, H. Vu, H. Sun, T.L. Pham, D.T. Nguyen, J.-S. Lee, J.G. Fisher, Growth of $(Na_{0.5}Bi_{0.5})TiO_3$-$SrTiO_3$ single crystals by solid state crystal growth, Ceram. Int. 42 (16) (2016) 18894–18901.

[30] P.G. Le, T.L. Pham, D.T. Nguyen, J.-S. Lee, J.G. Fisher, H.-P. Kim, W. Jo, Solid state crystal growth of single crystals of $0.75(Na_{1/2}Bi_{1/2})TiO_3$-$0.25SrTiO_3$ and their characteristic electrical properties, J. Asian Ceram. Soc. 9 (1) (2021) 40–51.

[31] S.J.L. Kang, J.H. Park, S.Y. Ko, H.Y. Lee, Solid-state conversion of single crystals: the principle and the state-of-the-art, J. Am. Ceram. Soc. 98 (2) (2015) 347–360.

[32] H. Sun, J.G. Fisher, S.H. Moon, H. Tran Tran, J.S. Lee, H.S. Han, H.P. Kim, W. Jo, Solid-state-growth of lead-free piezoelectric $(Na_{1/2}Bi_{1/2})TiO_3$-$CaTiO_3$ single crystals and their characterization, Mater. Sci. Eng., B 223 (2017) 109–119.

[33] P.G. Le, H.T. Tran, J.S. Lee, J.G. Fisher, H.P. Kim, W. Jo, W.J. Moon, Growth of Single Crystals in the $(Na_{1/2}Bi_{1/2})TiO_3$-$(Sr_{1-x}Ca_x)TiO_3$ System by Solid Sate Crystal Growth, J. Adv. Ceram., in press.

[34] H. Onozuka, Y. Kitanaka, Y. Noguchi, M. Miyayama, Crystal growth and characterization of $(Bi_{0.5}Na_{0.5})TiO_3$–$BaTiO_3$ single crystals obtained by a top-seeded solution growth method under high-pressure oxygen atmosphere, Jpn. J. Appl. Phys. 50 (9) (2011), 09NE07.

[35] S. Kong, N. Kumar, S. Checchia, C. Cazorla, J. Daniels, Defect-driven structural distortions at the surface of relaxor ferroelectrics, Adv. Funct. Mater. 29 (27) (2019) 1900344.

[36] M. Wojdyr, Fityk: a general-purpose peak fitting program, J. Appl. Crystallogr. 43 (5) (2010) 1126–1128.

[37] D. Schütz, M. Deluca, W. Krauss, A. Feteira, T. Jackson, K. Reichmann, Lone-pair-induced covalency as the cause of temperature- and field-induced instabilities in bismuth sodium titanate, Adv. Funct. Mater. 22 (11) (2012) 2285–2294.

[38] G. de la Flor, T. Malcherek, S. Gorfman, B. Mihailova, Structural transformations in $(1-x)Na_{0.5}Bi_{0.5}TiO_3$-$xBaTiO_3$ single crystals studied by Raman spectroscopy, Phys. Rev. B 96 (21) (2017) 214102.

[39] J. Kreisel, A.M. Glazer, G. Jones, P.A. Thomas, L. Abello, G. Lucazeau, An x-ray diffraction and Raman spectroscopy investigation of A-site substituted perovskite compounds: the $(Na_{1-x}K_x)_{0.5}Bi_{0.5}TiO_3$ $(0 \leq x \leq 1)$ solid solution, J. Phys. Condens. Matter 12 (14) (2000) 3267–3280.

[40] D. Rout, K.S. Moon, J. Park, S.J.L. Kang, High-temperature X-ray diffraction and Raman scattering studies of Ba-doped $(Na_{0.5}Bi_{0.5})TiO_3$ Pb-free piezoceramics, Curr. Appl. Phys. 13 (9) (2013) 1988–1994.

[41] X. Liu, S. Xue, J. Ma, J. Zhai, B. Shen, F. Wang, X. Zhao, H. Yan, Electric-field-induced local distortion and large electrostrictive effects in lead-free NBT-based relaxor ferroelectrics, J. Eur. Ceram. Soc. 38 (14) (2018) 4631–4639.

[42] D. Rout, K.S. Moon, V.S. Rao, S.J.L. Kang, Study of the morphotropic phase boundary in the lead-free $Na_{1/2}Bi_{1/2}TiO_3$-$BaTiO_3$ system by Raman spectroscopy, J. Ceram. Soc. Jpn. 117 (1367) (2009) 797–800.

[43] L. Jin, F. Li, S. Zhang, Decoding the fingerprint of ferroelectric loops: comprehension of the material properties and structures, J. Am. Ceram. Soc. 97 (1) (2014) 1–27.

[44] Y. Hiruma, H. Nagata, T. Takenaka, Phase diagrams and electrical properties of $(Bi_{1/2}Na_{1/2})TiO_3$-based solid solutions, J. Appl. Phys. 104 (12) (2008) 124106.

[45] J. Zang, M. Li, D.C. Sinclair, W. Jo, J. Rödel, Impedance spectroscopy of $(Bi_{1/2}Na_{1/2})TiO_3$–$BaTiO_3$ ceramics modified with $(K_{0.5}Na_{0.5})NbO_3$, J. Am. Ceram. Soc. 97 (5) (2014) 1523–1529.

[46] H.S. Han, I.K. Hong, Y.-M. Kong, J.S. Lee, W. Jo, Effect of Nb doping on the dielectric and strain properties of lead–free $0.94(Bi_{1/2}Na_{1/2})TiO_3$–$0.06BaTiO_3$ ceramics, J. Kor. Ceram. Soc. 53 (2) (2016) 145–149.

[47] S.M. An, B.K. Yoon, S.Y. Chung, S.J.L. Kang, Nonlinear driving force-velocity relationship for the migration of faceted boundaries, Acta Mater. 60 (11) (2012) 4531–4539.

[48] S.J.L. Kang, S.Y. Ko, S.Y. Moon, Mixed control of boundary migration and the principle of microstructural evolution, J. Ceram. Soc. Jpn. 124 (4) (2016) 259–267.

[49] P. Kabakov, C. Dean, V. Kurusingal, Z. Cheng, H.-Y. Lee, S. Zhang, Solid-state crystal growth of lead-free ferroelectrics, J. Mater. Chem. C 8 (2020) 7606–7649.

[50] Y.M. Chiang, D. Birnie, W.D. Kingery, Chapter 5 Microstructure, Physical Ceramics: Principles for Ceramic Science and Engineering, John Wiley & Sons, New York, 1997, pp. 351–513.

[51] A.A. Bokov, Z.-G. Ye, Recent progress in relaxor ferroelectrics with perovskite structure, J. Mater. Sci. 41 (1) (2006) 31–52.

[52] C.W. Ahn, C.H. Hong, B.Y. Choi, H.P. Kim, H.S. Han, Y. Hwang, W. Jo, K. Wang, J.F. Li, J.-S. Lee, I.W. Kim, A brief review on relaxor ferroelectrics and selected issues in lead-free relaxors, J. Kor. Phys. Soc. 68 (12) (2016) 1481–1494.

[53] D. Lee, H. Vu, H. Sun, T.L. Pham, D.T. Nguyen, J.-S. Lee, J.G. Fisher, Growth of $(Na_{0.5}Bi_{0.5})TiO_3$-$SrTiO_3$ single crystals by solid state crystal growth, Ceram. Int. 42 (2016), 188894-18901.

[54] Y. Hiruma, H. Nagata, T. Takenaka, Formation of morphotropic phase boundary and electrical properties of $(Bi_{1/2}Na_{1/2})TiO_3$–$Ba(Al_{1/2}Nb_{1/2})O_3$ solid solution ceramics, Jpn. J. Appl. Phys. 48 (9S1) (2009), 09KC08.

[55] A.R. Paterson, H. Nagata, X. Tan, J.E. Daniels, M. Hinterstein, R. Ranjan, P.B. Groszewicz, W. Jo, J.L. Jones, Relaxor-ferroelectric transitions: sodium bismuth titanate derivatives, MRS Bull. 43 (8) (2018) 600–606.

[56] A.A. Bokov, Z.-G. Ye, Dielectric relaxation in relaxor ferroelectrics, J. Adv. Dielectr. 2 (2) (2012) 1241010.

[57] V. Bobnar, A. Erste, U. Gradisar, C. Filipic, A. Levstik, Z. Kutnjak, High-temperature dielectric response of ferroelectric relaxors, IEEE Trans. Ultrason. Ferroelectrics Freq. Contr. 58 (11) (2011) 2270–2275.

[58] M. Vögler, N. Novak, F.H. Schader, J. Rödel, Temperature-dependent volume fraction of polar nanoregions in lead-free $(1-x)(Bi_{0.5}Na_{0.5})TiO_3$ - $xBaTiO_3$ ceramics, Phys. Rev. B 95 (2) (2017), 024104.

[59] G.O. Jones, P.A. Thomas, Investigation of the structure and phase transitions in the novel A-site substituted distorted perovskite compound $Na_{0.5}Bi_{0.5}TiO_3$, Acta Crystallogr. B 58 (2) (2002) 168–178.

[60] C.S. Tu, S.H. Huang, C.S. Ku, H.Y. Lee, R.R. Chien, V.H. Schmidt, H. Luo, Phase coexistence and Mn-doping effect in lead-free ferroelectric $(Na_{1/2}Bi_{1/2})TiO_3$ crystals, Appl. Phys. Lett. 96 (6) (2010) 1–3.

[61] F. Cordero, F. Craciun, F. Trequattrini, E. Mercadelli, C. Galassi, Phase transitions and phase diagram of the ferroelectric perovskite $(Na_{0.5}Bi_{0.5})_{1-x}Ba_xTiO_3$ by anelastic and dielectric measurements, Phys. Rev. B 81 (14) (2010) 144124.

[62] W. Jo, S. Schaab, E. Sapper, L.A. Schmitt, H.-J. Kleebe, A.J. Bell, J. Rödel, On the phase identity and its thermal evolution of lead free $(Bi_{1/2}Na_{1/2})TiO_3$-6 mol% $BaTiO_3$, J. Appl. Phys. 110 (7) (2011), 074106.

[63] H.-Y. Lee, K. Wang, F.-Z. Yao, W. Sun, Z. Zhou, M.-H. Zhang, X. Li, H. Luo, J.-S. Lee, J.-F. Li, Identifying phase transition behavior in $Bi_{1/2}Na_{1/2}TiO_3$-$BaTiO_3$ single crystals by piezoresponse force microscopy, J. Appl. Phys. 121 (17) (2017) 174103.

[64] F. Craciun, C. Galassi, R. Birjega, Electric-field-induced and spontaneous relaxor-ferroelectric phase transitions in $(Na_{1/2}Bi_{1/2})_{1-x}BaxTiO_3$, J. Appl. Phys. 112 (12) (2012) 124106.

[65] K. Reichmann, A. Feteira, M. Li, Bismuth sodium titanate based materials for piezoelectric actuators, Materials 8 (12) (2015) 5469.

[66] S. Gorfman, P.A. Thomas, Evidence for a non-rhombohedral average structure in the lead-free piezoelectric material $Na_{0.5}Bi_{0.5}TiO_3$, J. Appl. Crystallogr. 43 (6) (2010) 1409–1414.

[67] G.A. Smolenskii, V.A. Isupov, A.I. Agranovskaya, N.N. Krainik, New ferroelectrics of complex composition, Sov. Phys. Solid State 2 (1961) 2651–2654.

[68] C.F. Buhrer, Some properties of bismuth perovskites, J. Chem. Phys. 36 (3) (1962) 798–803.

[69] J.A. Zvirgzds, P.P. Kapostin, J.V. Zvirgzde, T.V. Kruzina, X-ray study of phase transitions in ferroelectric $Na_{0.5}Bi_{0.5}TiO_3$, Ferroelectrics 40 (1) (1982) 75–77.

[70] V. Dorcet, G. Trolliard, A transmission electron microscopy study of the A-site disordered perovskite $Na_{0.5}Bi_{0.5}TiO_3$, Acta Mater. 56 (8) (2008) 1753–1761.

[71] S. Gorfman, A.M. Glazer, Y. Noguchi, M. Miyayama, H. Luo, P.A. Thomas, Observation of a low-symmetry phase in $Na_{0.5}Bi_{0.5}TiO_3$ crystals by optical birefringence microscopy, J. Appl. Crystallogr. 45 (3) (2012) 444–452.

[72] S. Gorfman, D.S. Keeble, A. Bombardi, P.A. Thomas, Topology and temperature dependence of the diffuse X-ray scattering in $Na_{0.5}Bi_{0.5}TiO_3$ ferroelectric single crystals, J. Appl. Crystallogr. 48 (2015) 1543–1550.

[73] B.N. Rao, A.N. Fitch, R. Ranjan, Ferroelectric-ferroelectric phase coexistence in $Na_{1/2}Bi_{1/2}TiO_3$, Phys. Rev. B 87 (6) (2013), 060102.

[74] V.A. Shuvaeva, D. Zekria, A.M. Glazer, Q. Jiang, S.M. Weber, P. Bhattacharya, P.A. Thomas, Local structure of the lead-free relaxor ferroelectric $(K_xNa_{1-x})_{0.5}Bi_{0.5}TiO_3$, Phys. Rev. B 71 (17) (2005) 174114.

[75] P.B. Groszewicz, M. Gröting, H. Breitzke, W. Jo, K. Albe, G. Buntkowsky, J. Rödel, Reconciling local structure disorder and the relaxor state in $(Bi_{1/2}Na_{1/2})TiO_3$-$BaTiO_3$, Sci. Rep. 6 (1) (2016) 31739.

[76] B.N. Rao, R. Datta, S.S. Chandrashekaran, D.K. Mishra, V. Sathe, A. Senyshyn, R. Ranjan, Local structural disorder and its influence on the average global structure and polar properties in $Na_{0.5}Bi_{0.5}TiO_3$, Phys. Rev. B 88 (22) (2013) 224103.

[77] D. Rout, K.S. Moon, S.J.L. Kang, I.W. Kim, Dielectric and Raman scattering studies of phase transitions in the $(100-x)Na_{0.5}Bi_{0.5}TiO_3$–$xSrTiO_3$ system, J. Appl. Phys. 108 (8) (2010), 084102.

[78] S. Kim, H. Choi, S. Han, J.S. Park, M.H. Lee, T.K. Song, M.-H. Kim, D. Do, W.-J. Kim, A correlation between piezoelectric response and crystallographic structural parameter observed in lead-free $(1-x)(Bi_{0.5}Na_{0.5})TiO_3$–$xSrTiO_3$ piezoelectrics, J. Eur. Ceram. Soc. 37 (4) (2017) 1379–1386.

[79] Y. Hiruma, H. Nagata, T. Takenaka, Detection of morphotropic phase boundary of $(Bi_{1/2}Na_{1/2})TiO_3$–$Ba(Al_{1/2}Sb_{1/2})O_3$ solid-solution ceramics, Appl. Phys. Lett. 95 (5) (2009), 052903.

[80] R.D. Shannon, Revised effective ionic radii and systematic studies of interatomic distances in halides and chalcogenides, Acta Crystallogr. A 32 (5) (1976) 751–767.

[81] A.R. West, Crystal Defects, Non - Stoichiometry and Solid Solutions, Solid State Chemistry and its Applications, second ed., John Wiley & Sons Ltd., Chichester, 2014, pp. 87–124.

[82] W. Bai, L. Li, W. Li, B. Shen, J. Zhai, H. Chen, Phase diagrams and electromechanical strains in lead-free BNT-based ternary perovskite compounds, J. Am. Ceram. Soc. 97 (11) (2014) 3510–3518.

[83] W. Bai, B. Shen, J. Zhai, F. Liu, P. Li, B. Liu, Y. Zhang, Phase evolution and correlation between tolerance factor and electromechanical properties in BNT-based ternary perovskite compounds with calculated end-member $Bi(Me_{0.5}Ti_{0.5})O_3$ (Me = Zn, Mg, Ni, Co), Dalton Trans. 45 (36) (2016) 14141–14153.

[84] W. Bai, D. Chen, P. Zheng, J. Zhang, F. Wen, B. Shen, J. Zhai, Z. Ji, Phase transition, switching characteristics of MPB compositions and large strain in lead-free $(Bi_{0.5}Na_{0.5})TiO_3$-based piezoceramics, J. Alloys Compd. 709 (2017) 646–657.

[85] C. Luo, W. Ge, Q. Zhang, J. Li, H. Luo, D. Viehland, Crystallographic direction dependence of direct current field induced strain and phase transitions in $Na_{0.5}Bi_{0.5}TiO_3$-x%$BaTiO_3$ single crystals near the morphotropic phase boundary, Appl. Phys. Lett. 101 (14) (2012) 141912.

[86] D. Schneider, W. Jo, J. Rödel, D. Rytz, T. Granzow, Anisotropy of ferroelectric behavior of $(1-x)Bi_{1/2}Na_{1/2}TiO_3$–$xBaTiO_3$ single crystals across the morphotropic phase boundary, J. Appl. Phys. 116 (4) (2014), 044111.

[87] W. Jo, R. Dittmer, M. Acosta, J. Zang, C. Groh, E. Sapper, K. Wang, J. Rödel, Giant electric-field-induced strains in lead-free ceramics for actuator applications – status and perspective, J. Electroceram. 29 (1) (2012) 71–93.

[88] J.E. Daniels, W. Jo, J. Rödel, J.L. Jones, Electric-field-induced phase transformation at a lead-free morphotropic phase boundary: case study in a 93%$(Bi_{0.5}Na_{0.5})TiO_3$–7%$BaTiO_3$ piezoelectric ceramic, Appl. Phys. Lett. 95 (3) (2009), 032904.

[89] M. Hinterstein, M. Knapp, M. Hölzel, W. Jo, A. Cervellino, H. Ehrenberg, H. Fuess, Field-induced phase transition in $Bi_{1/2}Na_{1/2}TiO_3$-based lead-free piezoelectric ceramics, J. Appl. Crystallogr. 43 (6) (2010) 1314–1321.

[90] K. Wang, A. Hussain, W. Jo, J. Rödel, Temperature-dependent properties of $(Bi_{1/2}Na_{1/2})TiO_3$–$(Bi_{1/2}K_{1/2})TiO_3$–$SrTiO_3$ lead-free piezoceramics, J. Am. Ceram. Soc. 95 (7) (2012) 2241–2247.

[91] A. Ullah, H.B. Gul, A. Ullah, M. Sheeraz, J.-S. Bae, W. Jo, C.W. Ahn, I.W. Kim, T.H. Kim, Giant room-temperature electrostrictive coefficients in lead-free relaxor ferroelectric ceramics by compositional tuning, Apl. Mater. 6 (1) (2018), 016104.

[92] J.S. Lee, A superior description of AC behavior in polycrystalline solid electrolytes with current-constriction effects, J. Kor. Ceram. Soc. 53 (2) (2016) 150–161.

[93] J.-S. Lee, J. Jamnik, J. Maier, Generalized equivalent circuits for mixed conductors: silver sulfide as a model system, Monatshefte für Chemie - Chem. Monthly 140 (9) (2009) 1113–1119.

[94] M. Li, M.J. Pietrowski, R.A. De Souza, H.R. Zhang, I.M. Reaney, S.N. Cook, J.A. Kilner, D.C. Sinclair, A family of oxide ion conductors based on the ferroelectric perovskite $Na_{0.5}Bi_{0.5}TiO_3$, Nat. Mater. 13 (1) (2014) 31–35.

[95] J.H. Kim, E.C. Shin, D.C. Cho, S. Kim, S. Lim, K. Yang, J. Beum, J. Kim, S. Yamaguchi, J.S. Lee, Electrical characterization of polycrystalline sodium β″-alumina: revisited and resolved, Solid State Ionics 264 (2014) 22–35.

[96] H.T. Nguyen, T.L. Tran, D.T. Nguyen, E.-C. Shin, S.-H. Kang, J.-S. Lee, Full parametric impedance analysis of photoelectrochemical cells: case of a $TiO_2$ photoanode, J. Kor. Ceram. Soc. 55 (3) (2018) 244–260.

[97] H. Seo, K. Jin, S. Park, K.H. Cho, H. Ha, K.-G. Lee, Y.H. Lee, D.T. Nguyen, H. Randriamahazaka, J.-S. Lee, K.T. Nam, Mechanistic investigation with kinetic parameters on water oxidation catalyzed by manganese oxide nanoparticle film, ACS Sustain. Chem. Eng. 7 (12) (2019) 10595–10604.

[98] S.H. Moon, Y.H. Kim, D.C. Cho, E.C. Shin, D. Lee, W.B. Im, J.S. Lee, Sodium ion transport in polymorphic scandium NASICON analog $Na_3Sc_2(PO_4)_3$ with new dielectric spectroscopy approach for current-constriction effects, Solid State Ionics 289 (2016) 55–71.

[99] J.R. Macdonald, Universality, the Barton Nakajima Namikawa relation, and scaling for dispersive ionic materials, Phys. Rev. B 71 (18) (2005) 184307.